

The Sunyaev Zel'dovich effect: simulations and observations

Zhang, Pengjie

Department of Astronomy & Astrophysics, University of Toronto, M5S 3H8, Canada

zhangpj@cita.utoronto.ca

Pen, Ue-Li

Canadian Institute for Theoretical Astrophysics, University of Toronto, M5S 3H8, Canada

pen@cita.utoronto.ca

Wang, Benjamin

Physics and Astronomy Department, University of British Columbia, Canada

ABSTRACT

The Sunyaev Zel'dovich effect (SZ effect) is a complete probe of ionized baryons, the majority of which are likely hiding in the intergalactic medium. We ran a 512^3 Λ CDM simulation using a moving mesh hydro code to compute the statistics of the thermal and kinetic SZ effect such as the power spectra and measures of non-Gaussianity. The thermal SZ power spectrum has a very broad peak at multipole $l \sim 2000 - 10^4$ with temperature fluctuations $\Delta T \sim 15 \mu\text{K}$. The power spectrum is consistent with available observations and suggests a high $\sigma_8 \simeq 1.0$ and a possible role of non-gravitational heating. The non-Gaussianity is significant and increases the cosmic variance of the power spectrum by a factor of ~ 5 for $l < 6000$.

We explore optimal driftscan survey strategies for the AMIBA CMB interferometer and their dependence on cosmology. For SZ power spectrum estimation, we find that the optimal sky coverage for a 1000 hours of integration time is several hundred square degrees. One achieves an accuracy better than 40% in the SZ measurement of power spectrum and an accuracy better than 20% in the cross correlation with Sloan galaxies for $2000 < l < 5000$. For cluster searches, the optimal scan rate is around 280 hours per square degree with a cluster detection rate 1 every 7 hours, allowing for a false positive rate of 20% and better than 30% accuracy in the cluster SZ distribution function measurement.

Subject headings: Cosmology-theory-simulation-observation: SZ effect, cosmic microwave background, large scale structure, cluster.

1. Introduction

Big bang nucleosynthesis (BBN) and cosmic microwave background (CMB) experiments such as Boomerang (Netterfield et al. 2001) and DASI (Pryke et al. 2001) predict that the ordinary baryonic matter accounts for about 5% of the total matter in the universe. But the directly observed components, such as stars, interstellar medium and intracluster gas, only account for a few percent of this baryon budget, while more than 90% baryons have escaped direct detections (Persic & Salucci 1992; Fukugita, Hogan & Peebles 1998). This is known as the missing baryon problem. The missing baryons are believed to be in the form of the intergalactic medium (IGM) and have been difficult to detect directly. To understand their state, such as density, temperature, peculiar velocity and metallicity, stands as a major challenge to both observation and theory, and is crucial to understand the thermal history of the universe and galaxy formation.

The IGM has various direct observable tracers. (1) Neutral hydrogen absorbs background light of quasars and produces the Lyman- α forest. (2) Ionized electrons have thermal and peculiar motions and are capable of scattering CMB photons and generate secondary CMB temperature fluctuations, which are known as the thermal and kinetic Sunyaev Zel’dovich effects (SZ effect), respectively. Their precision measurements are becoming routinely available with the devoted CMB experiments such as AMIBA (Array for MICrowave Background Anisotropy 2003) and SZA (Sunyaev Zel’dovich array). (3) Ionized electrons and protons interact with each other and emit X-rays through thermal bremsstrahlung and contribute to the soft X-ray (0.5 – 2 keV) background (XRB). Several other tracers have been proposed, including X-ray absorption techniques (Perna & Loeb 1998), but they depend strongly on chemical compositions, and would be difficult to associate with direct IGM properties. These tracers probe different IGM phases and help to extract the IGM state. For example, the XRB flux upper limits place constrain on the gas clumpyness and suggest a potentially strong role of feedback (Pen 1999).

Among these tracers, the SZ effect is a particularly powerful IGM probe. (1) It provides a complete sample of the intergalactic medium. All free electrons participate in Thomson scattering and contribute to the SZ effect. The Thomson optical depth from the epoch of reionization $z \sim 10$ to the present is $\tau \sim 0.1$, which means that about 10% of CMB photons have been scattered by electrons. Since the number of CMB photons is much larger than the baryon number and the ionization fraction of our universe is larger than 99%, most baryons contribute to the SZ effect. Compton scattering does not depend on redshift and is not affected by distance or the expansion of the universe. So, the SZ effect can probe the distant universe. Furthermore, the SZ effect does not strongly depend on gas density and probes a large dynamic range of baryon fluctuations. In contrast, the X-ray emission measure depends on density squared, and primarily probes the densest IGM regions at low redshift. The Lyman- α forest probes the neutral IGM, which in ionization equilibrium depends also on the square of the baryon density. The neutral fractions only accounts for a tiny fraction of total baryons. Extrapolations over many orders of magnitude are required to understand the bulk of the baryons. (2) It is straightforward to understand. The simple dependence of the SZ effect on the ionized gas pressure or momentum does not put as stringent

requirement on simulation resolution, nor as accurate an understanding of the gas state such as metallicity, temperature, velocity and ionization equilibrium, as X-rays and Lyman- α properties do. Pressure is the total thermal energy content of the gas, and finite volume flux conservative simulations are particularly amenable to its modelling. It is also easier to model analytically. (3) It has strong observational potential. In this paper we will primarily consider the thermal SZ effect, which is easier to observe. Its unique dependence on frequency allows us in principle to disentangle the SZ effect from the contamination of the primary CMB and other noise sources (Cooray, Hu & Tegmark 2000). Hereafter, if not otherwise specified, the SZ effect always means the thermal SZ effect.

In SZ observations, all redshifts are entangled and smear some key information of the intervening IGM: its spatial distribution and time evolution. These properties around redshift $z \sim 1$ are sensitive to many cosmological parameters and thus potentially promising to break degeneracies in cosmologies from the primary CMB experiments. One can hope to resolve the equation of the state of the dark energy. We are currently performing simulations for different cosmologies, which are degenerate in the primary CMB, to test the potential of such a procedure (Zhang et al. 2002). If combined with other observations, the SZ effect will become even more powerful. For example, with the aid of a galaxy photometric redshift survey, the evolution of the 3D gas pressure power spectrum and its cross correlation with the galaxy distribution can be extracted (Zhang & Pen 2001).

The above analysis depends on a detailed quantitative theoretical understanding of the SZ statistics. Analytical approaches considered in the past strongly depend on various assumptions. The Press-Schechter approach as adopted by Cole & Kaiser (1988); Makino & Suto (1993); Atrio-Barandela & Mucket (1999); Komatsu & Kitayama (1999); Cooray (2000); Molnar & Birkinshaw (2000) requires ad hoc models for the gas profile in halos, whose shape and evolution are uncertain. The hierarchical method as proposed by Zhang & Pen (2001) strongly depends on the gas-dark matter correlation, which is also poorly understood. These estimates can be significantly improved by high-resolution simulations. But past simulation results (Scaramella et al. 1993; da Silva et al. 2000; Refregier et al. 2000; Seljak, Burwell & Pen 2001; Springel et al. 2001) disagreed on both amplitude and shape of the SZ power spectrum (see Springel et al. (2001) for a recent discussion). Simulation resolution may play a key role in this discrepancy since the SZ effect is sensitive to small structures, as discussed by Seljak, Burwell & Pen (2001). Differences between code algorithms may also cause part of the discrepancy. To address these problems, we ran the largest adaptive SZ simulation to date, a direct 512^3 moving mesh hydro (MMH) code (Pen 1998a) simulation, to reinvestigate the SZ statistics. For a better understanding of numerical and code issues in the SZ effect, our group is carrying out a series of simulations with identical cosmological parameters and initial condition but using different codes with different resolutions (Codes Comparison Program 2002).

Apart from simulation issues, a problem that has received little attention is analysis strategies for SZ data. Several interferometric arrays such as AMIBA and SZA are under construction, but

detailed data analysis models are still in their infancy. With our simulated SZ maps, we can estimate the sensitivity and accuracy of SZ observations. Given a sky scan rate, how accurately can the SZ power spectrum be measured? How many cluster can be found? How accurately can the SZ decrement be determined for individual clusters? What are optimal strategies for these measurements? In this paper, we will take AMIBA as our target to address these questions.

This paper is organized as follows: in §2, we describe the SZ effect, its statistics and our method to analyze these statistics. We then present our simulation results of these statistics and possible constrain from observations (§3). In §4 we simulate AMIBA driftscan observations to estimate the accuracy of AMIBA measurement of these statistics. We conclude in §5.

2. Formulation and Background Review

The thermal SZ effect causes CMB temperature and intensity fluctuations in the sky. At a given position given by a unit vector \hat{n} pointing from the earth to some point on the sky, the fractional change in the CMB intensity $\delta I_\nu/I_\nu$ depends on both the observing frequency ν and the integral of the gas pressure along the line of sight (Zel'dovich and Sunyaev 1969):

$$\frac{\delta I_\nu}{I_\nu} = -2y(\hat{n})S_I[x(\nu)]. \quad (1)$$

For the CMB intensity, the spectral dependence for inverse compton scattering off non-relativistic electrons is described by $S_I(x) = \frac{xe^x}{e^x-1} (2 - x/[2 \tanh(x/2)])$ where $x \equiv h\nu/(k_B T_{\text{CMB}}) = \nu/57 \text{ GHz}$. The corresponding fractional change in CMB temperature $\Theta(\hat{n}) \equiv \frac{\Delta T_{\text{CMB}}(\hat{n})}{T_{\text{CMB}}}$ is then:

$$\Theta(\hat{n}, \nu) = -2y(\hat{n})S_T[x(\nu)] = -2y(2 - x/[2 \tanh(x/2)]). \quad (2)$$

In the Rayleigh-Jeans limit ($x \ll 1$), $S_I(x) = S_T(x) = 1$. $S_I(x)$ reaches the highest response, $S(x) \simeq 1.6$ at $\nu \simeq 100 \text{ GHz}$, which is well matched to the AMIBA frequency range of 80-100 GHz. $S_T(x)$ monotonously decreases with frequency. We show $S_I(x)$ and $S_T(x)$ in fig. (1) where the frequency responses of various experiments which already have the CMB observation data at small angular scales ($l > 2000$) such as ATCA (Subrahmanyam et al. 2000), BIMA (Dawson et al. 2001), CBI¹, SUZIE (Church et al. 1997) and VLA (Partridge et al. 1997) are shown. The gas pressure dependence is described by the Compton y parameter

$$y(\hat{n}) = \frac{\sigma_T}{m_e c^2} \int_0^{l_{\text{re}}} n_e(l\hat{n}) k_B T_e(l\hat{n}) dl = \frac{\sigma_T}{m_e c^2} \int_0^{l_{\text{re}}} P_e(l\hat{n}) dl. \quad (3)$$

T_e , n_e and P_e are the temperature, number density and pressure of free electrons, respectively. dl is the proper distance interval along the path of CMB photons. σ_T , m_e and c have their usual meanings as the Thomson cross section, electron mass and the speed of light. Since only free electrons participate in Thomson scattering of the CMB photons, the integral is cut off at the epoch of reionization l_{re} .

¹<http://www.astro.caltech.edu/~tjp/CBI/>

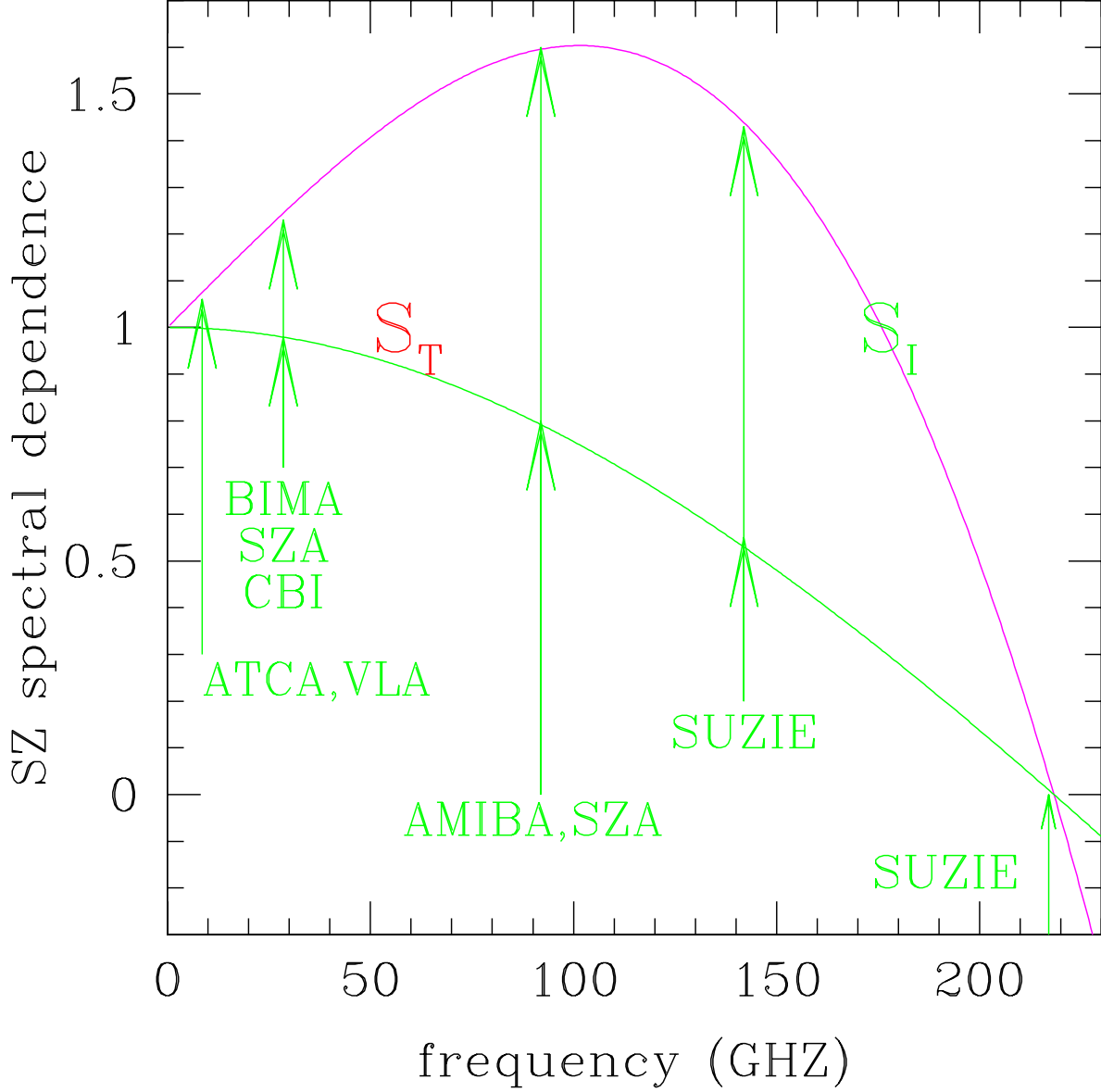


Fig. 1.— The SZ spectral dependence of CMB brightness fluctuation $S_I(\nu)$ and temperature fluctuation $S_T(\nu)$. $\delta I_\nu / I_\nu^{\text{CMB}} = -2yS_I(\nu)$. $\Delta T / T_{\text{CMB}} = -2yS_T(\nu)$. We show the responses of various experiments which are capable of detecting SZ signals such as AMIBA: 90 GHz (Array for Microwave Background Anisotropy 2003), ATCA: 8.7 GHz (Subrahmanyan et al. 2000), BIMA: 28.5 GHz (Dawson et al. 2001), CBI: 26-36 GHz, SUZIE: 142 GHz, 217 GHz, etc. (Church et al. 1997), SZA: 26-36 GHz and 85-115 GHz and VLA: 8.4 GHz (Partridge et al. 1997). $S(\nu) \rightarrow 1$ when $\nu \ll 50$ GHz. At 217 GHz, there is no thermal SZ effect, enabling the measurement of other CMB anisotropies such as the kinetic SZ effect.

Some important statistics of the SZ effect immediately come to mind. The first order quantity is \bar{y} , the mean y parameter averaged over the whole sky, which measures the total thermal energy content of the universe. The angular variation in y can be parameterized by the two point correlation function of the temperature fluctuation Θ , or equivalently the angular power spectrum C_l . For a Gaussian random field, these two parameters would describe the statistics completely. Since the SZ effect is dominated by non-linear structures, non-Gaussianity may be significant. So we investigate higher order statistics such as the skewness and kurtosis of the y parameter to quantify the non-Gaussianity.

The SZ effect contains contributions from all redshifts and it is challenging to recover the smeared redshift information. We have shown that cross correlating the SZ effect with a galaxy photometric redshift survey, we can infer the redshift resolved IGM pressure-galaxy cross correlation and the IGM pressure auto correlation (Zhang & Pen 2001). This method is robust, but does not capture all the information in the SZ observation. In this paper, we utilize the one point distribution function (PDF) of the y parameter and the distribution of peaks in y to extract more information.

Since smoothing is always present for a real experiment with a finite beam, we calculate the statistics of the y parameter smoothed on a given angular scale θ . If we are interested in virialized objects, for example clusters and groups of galaxies, we would expect them to be peaks in the smoothed or filtered y maps. $N(y > y_p)$, the cumulative distribution function (CDF) of peaks with smoothed y parameter bigger than certain value y_p , is the raw observable. The y_p CDF is the SZ analog to a luminosity function. If we choose a top hat window so that the observation cone is large enough to include an entire object such as a cluster and is small enough that typically no more than one such object can be found along each cone, then when the cone is centered at the center of each object, a peak $y \equiv y_p$ appears in the smoothed map. This y_p is directly related to the total gas mass and temperature of individual object. Assuming a halo to be isothermal, the total mass M of a halo is related to the gas temperature T by $M/M_8 = (T/T_8)^{3/2}$. $M_8 = 1.8 \times 10^{14} (\Omega_0/0.3) h^{-1} M_\odot$ is the mass contained in a $8h^{-1}\text{Mpc}$ sphere of the universe of mean density today, which is roughly the mass scale of clusters. $T_8(z)$ is the corresponding temperature of a halo with mass M_8 at redshift z . We then obtain

$$y_p = \frac{M_8 f_g}{\mu m_H} \frac{\sigma_T}{d_A^2 \Delta\Omega} \frac{k_B T_8}{m_e c^2} \left(\frac{M}{M_8} \right)^{5/3}. \quad (4)$$

Here, $\Delta\Omega$ is the solid angle of the cone, f_g is the gas fraction of halos and d_A is the angular diameter distance. For clusters and groups, the typical angular size at $z = 1$ is about $1'$. For the present cluster number density $n(T > 2\text{keV}) \sim 10^{-5} h^{-3} \text{Mpc}^3$ (Pen 1998b), the average number of clusters in a cone with angular radius $\theta \sim 20'$ projected to $z \sim 2$ is about one allowing for the evolution of cluster number density. So, the size of the smoothing scale for the peak analysis should be between these two scales. In this case, the $N(y > y_p)$ is just the number of halos with $y > y_p$, which is given by:

$$N(y > y_p) = \int_0^{r_{\text{re}}} \chi^2 dr / \sqrt{1 - Kr^2} \int_{M(y_p, z)}^\infty \frac{dn}{dM} dM. \quad (5)$$

$\frac{dn}{dM}(M, z)$ is the halo comoving number density distribution function and is well described by the

Press-Schechter formalism (Press & Schechter 1974). χ , r and K are the comoving distance, radial coordinate and curvature of the universe, respectively. The subscript ‘re’ means the reionization epoch. $M(y_p, z)$ is the mass of the halo with smoothed $y = y_p$ given by eqn. (4). Eqn. (5) has two applications. Firstly, given a SZ survey and the best constrained cosmological parameters as determined by CMB experiments, Type Ia SN, weak lensing, etc. and a SZ survey, the only unknown variable in eqn. (5) is $T_8(z)f_g(z)$, which then is uniquely determined. T_8 is robustly predicted since it is mainly determined by M_8 through hydrostatic equilibrium and has only weak dependence on the thermal history. For example, comparing the cluster temperature function as inferred from simulations with the Press-Schechter formalism, Pen (1998b) found that $T_8 = 4.9(1+z)\Omega_0^{2/3}\Omega(z)^{0.283}\text{keV}$ for a ΛCDM universe. The above relation is sufficient to extract the evolution of the gas fraction f_g , which is very sensitive to the thermal history. For example, non-gravitational energy injection decreases f_g . Secondly, the number of clusters strongly depends on cosmology, as characterized by $\frac{dn}{dM}$. Given a good understanding of cluster temperature and gas fraction, eqn. (5) allows one to constrain cosmological parameters. In combination with the measurement of cluster redshifts, this method is more sensitive (Weller, Battye & Kneissl 2001). In §4, we will study the statistics of these peaks for maps filtered in optimal ways to measure clusters of galaxies.

With the measurement of the cluster SZ temperature distortion and follow up X-ray observations of cluster X-ray flux F_X and X-ray temperature T , cosmological parameters can be constrained. For a cluster with electron number density n_e , proper size L and angular size θ , $F_X \propto n_e^2 \Lambda(T) L^3 / d_L^2$ and $y \propto n_e T L$. Here, $\Lambda(T)$ is the X-ray emissivity temperature dependence. Then the luminosity distance $d_L(z) \propto \frac{y^2}{F_X} \frac{\Lambda(T)}{T^2} \frac{\theta}{(1+z)^2}$. The only uncertainties in this relation are the intracluster gas profile and metallicity which affects the X-ray emissivity. These properties could be modelled and are potentially observable. In this sense, the SZ effect can be used as a cosmological distance indicator (Silk & White 1978; Barbosa et al. 1996; Mason, Myers & Readhead 2001; Fox & Pen 2001). Since dark energy dominates at low redshift where the SZ observation and X-ray observation of clusters are relatively straightforward, SZ clusters are a potential probe to constrain the equation of state for the dark energy.

3. Simulations

In this section, we describe our SZ simulation used to investigate the above statistics. We will also use our simulation to provide SZ maps for our estimation of the sensitivity of upcoming SZ experiments (§4) and its effect on data analysis strategies. We used a moving mesh hydrodynamics (MMH) code (Pen 1998a). It features a full curvilinear total-variation-diminishing (TVD) hydro code with a curvilinear particle mesh (PM) N-body code on a moving coordinate system. The full Euler equations are solved in an explicit flux-conservative form using a second order TVD scheme. The curvilinear coordinates used in the code are derived from a gradient of the Cartesian coordinate system. If x^i are the Cartesian coordinates, the curvilinear coordinates are $\xi^i = x^i + \partial_\xi^i \phi(\xi)$. The

transformation is completely specified by the single potential field $\phi(\xi, t)$. The potential deformation maintains a very regular grid structure in high density regions. The gravity and grid deformation equations are solved using a hierarchical multigrid algorithm for linear elliptic equations. These are solved in linear time, and are asymptotically faster than the FFT gravity solver. At the same time, adaptive dynamic resolution is achieved. During the evolution any one constraint can be satisfied by the grid. In our case, we follow the mass field such that the mass per unit grid cell remains approximately constant. This gives all the dynamic range advantages of smooth particle hydro (SPH) combined with the speed and high resolution of grid algorithms. The explicit time integration limits the time step by the Courant condition. To achieve a reasonable run time, we limit the compression factor to a factor of 5 in length, corresponding to a factor of 125 in density. Most SZ contributions arise below such densities, giving a diminishing return to go to higher compression factors.

The parameters we adopted in our 512^3 simulation are $\Omega_0 = 0.37$, $\Omega_\Lambda = 0.63$, $\Omega_B = 0.05$, $h = 0.7$, $\sigma_8 = 1.0$, power spectrum index $n = 1$, box size $L = 100h^{-1}$ Mpc and smallest grid spacing $40h^{-1}$ kpc. The simulation used 30 GB memory and took about three weeks (~ 1500 steps) on a 32 processor shared memory Alpha GS320 at CITA using Open MP parallelization directives. During the simulation we store 2D projections through the 3D box at every light crossing time through the box. The projections are made alternatively in the x, y, z directions to minimize the repetition of the same structures in the projection. We store projections of thermal SZ, kinetic SZ, gas and dark matter densities. For the thermal SZ, we store $2\Delta y = \frac{2\sigma_T}{m_e c^2} P_e L$ as given by eqn. (3). Our 2D maps are stored on 2048^2 grids. As tested by Seljak, Burwell & Pen (2001), this preserves all the information down to the finest grid spacing. After the simulation, we stack the SZ sectional maps separated by the width of simulation box, randomly choosing the center of each section and randomly rotating and flipping each section. The periodic boundary condition guarantees that there are no discontinuities in any of the maps. We then add these sections onto a map of constant angular size. Using different random seeds for the alignments and rotations, we make 40 maps of width 1.19 degrees to calculate the SZ statistics. The mean y parameter in these 40 maps $\bar{y} \simeq 4 \times 10^{-6}$. The mean y parameter is still below the upper limit 1.5×10^{-5} from COBE FIRAS (Fixsen et al. 1996). One typical thermal SZ sky map and a kinetic SZ sky map at the same field of view are shown in fig. 2 and fig. 3, respectively. With these maps, we calculate the SZ power spectrum, the SZ non-Gaussianity, the y PDF and y_p CDF.

3.1. The SZ power spectrum

The power spectrum in the Rayleigh-Jeans regime averaged over 40 maps is shown in fig. 4. The thermal SZ power spectrum is fairly flat, with a broad peak at $l \sim 2000$ - 10^4 and a typical fluctuation amplitude $\Theta \sim 5.5 \times 10^{-6}$. It begins to dominate over the primary CMB at $l \sim 2000$. The shape of the kinetic SZ power spectrum is similar to the thermal one but the amplitude is about 30 times smaller.

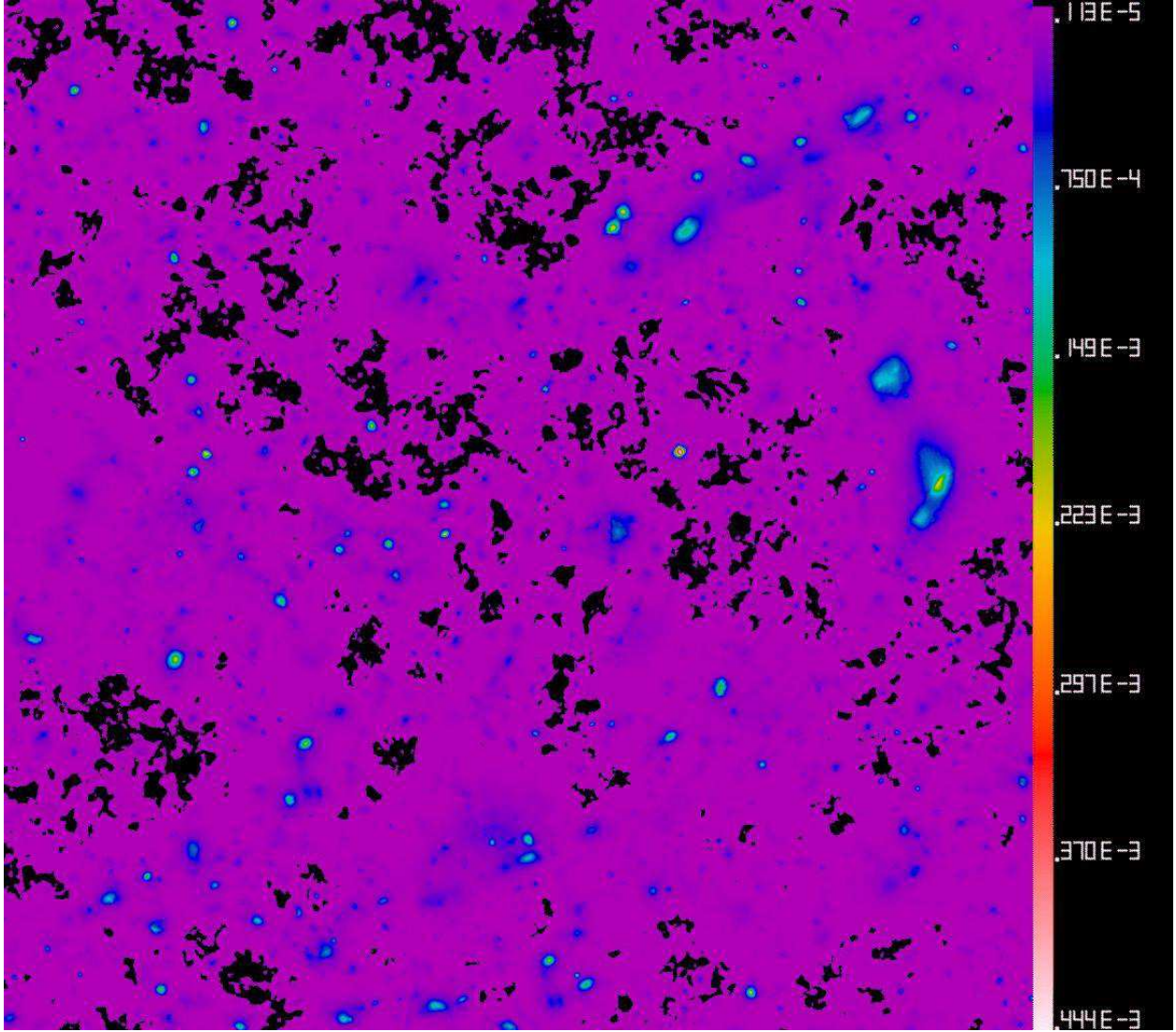


Fig. 2.— One typical thermal SZ map in our moving mesh hydro (MMH) code simulation. The cosmology is a Λ CDM with $\Omega_0 = 0.37$, $\Omega_\Lambda = 0.63$, $\Omega_B = 0.05$, $h = 0.7$ and $\sigma_8 = 1.0$. The map size is $1.19^\circ \times 1.19^\circ$. The color represents the SZ temperature fluctuation in the Rayleigh-Jeans regime $\Delta T/T = -2y$. We have omitted the negative sign. The SZ map clearly shows the structures with angular scale $\sim 1'$, which is the typical scale of clusters and groups.

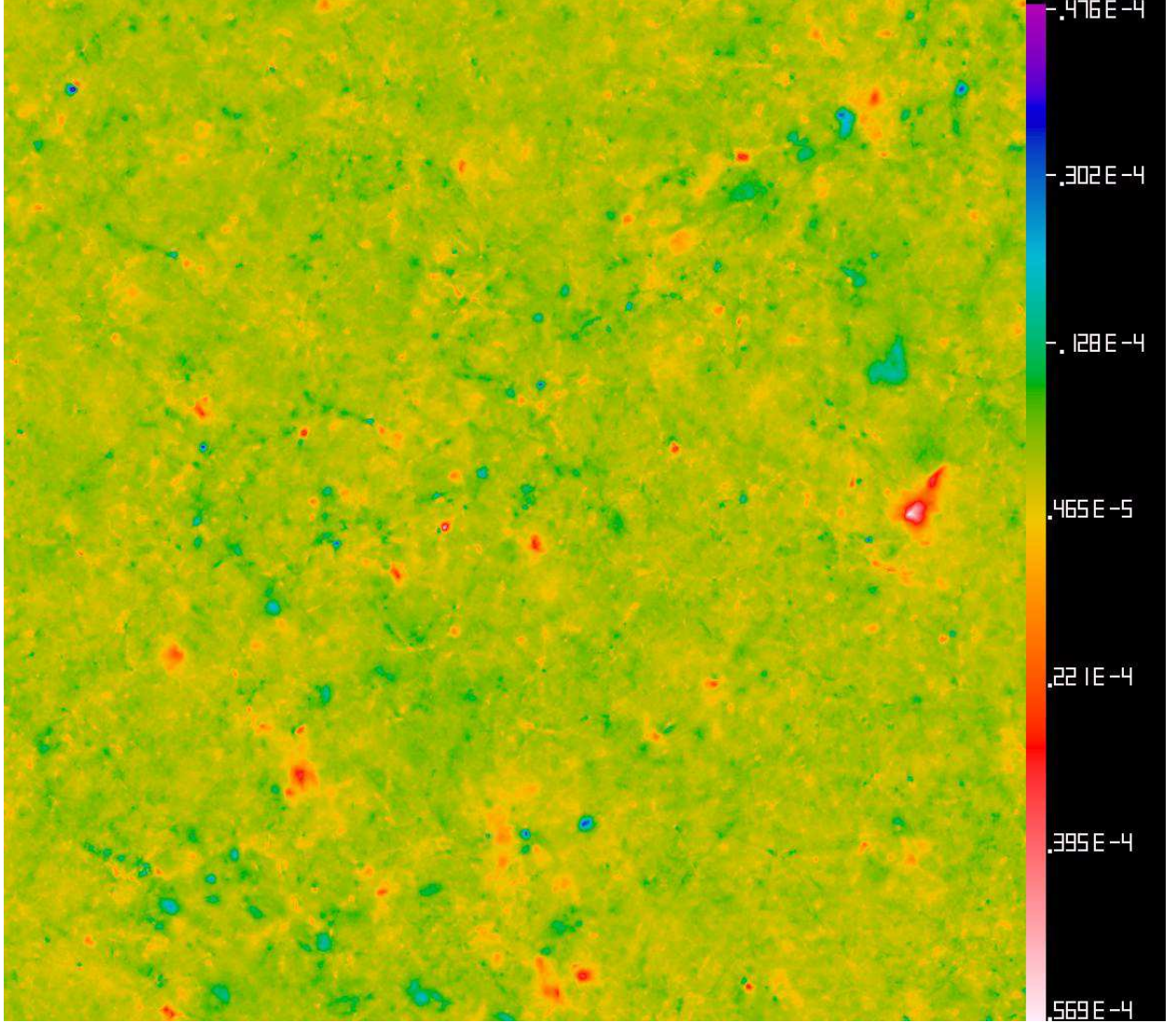


Fig. 3.— The kinetic SZ map in the same simulation at the same field of view as fig. 2. The amplitude of temperature fluctuation of the kinetic SZ effect is generally one order of magnitude lower than the thermal SZ effect. Gas in the positive $\Delta T/T$ regions is approaching us and those in the negative $\Delta T/T$ regions is moving away.

Comparing to available CMB observations, our thermal SZ power spectrum is well below the upper limit (95% confidence) of ATCA (Subrahmanyam et al. 2000), SUZIE (Church et al. 1997) and VLA (Partridge et al. 1997). C_l at $l \sim 2000$ is consistent with recent indications from the CBI experiment (Mason et al. 2001; Sievers et al. 2001) and may suggest a high $\sigma_8 \simeq 1.0$. But our result is higher than the BIMA 1- σ result though it is consistent with the upper limit (95% confidence) of the BIMA result (Dawson et al. 2001). We will further discuss these issues below.

Published theoretical predictions differ a lot in both amplitude and shape (see Springel et al. (2001) for a review). Our power spectrum has a higher amplitude than all previous predictions. It is also significantly flatter at the range $2000 < l < 15000$. The difference in amplitude can be explained by the strong dependence of the SZ effect on cosmological parameters, especially σ_8 . One expects $y \propto \Omega_B h \sigma_8^{2-3}$ and $C_l \propto (\Omega_B h)^2 \sigma_8^{6-9}$ as predicted by various authors (Komatsu & Kitayama 1999; Seljak, Burwell & Pen 2001; Zhang & Pen 2001). For example, Seljak, Burwell & Pen (2001) used the same MMH code with lower resolution (256^3) to simulate a universe with $\sigma_8 = 0.8$. This σ_8 difference accounts for a factor of $1.6 \sim 2.0$ difference in the mean \bar{y} estimation and $3.8 \sim 7.5$ difference in the C_l estimation. After accounting for these effects, our power spectrum is consistent with theirs at small angular scales ($l > 3000$). But the difference in shape can not be explained in this way. For example, even after accounting for the effect of cosmological parameters, our power spectrum is still much larger at large angular scales ($l \sim 1000$) than that of Seljak, Burwell & Pen (2001) (at $l \sim 1000$, ~ 2 times larger). This flatness behavior may be a manifestation of the resolution effect.

We notice that there are numerous high y regions of arcminute or sub-arcminute scales in SZ maps as seen in fig. 2. To quantify this phenomenon, we show the dependence of $N_\theta(y > y_p)$ on smoothing angular size θ (fig. 5). $N_\theta(y > y_p)$ is a measure of number of structures with angular size larger than or comparable to θ . Fig. 5 shows that when the smoothing scale increases from $0.5'$ to $1'$, $N(y > y_p)$ drops significantly in high y regions. This behavior suggests the existence of numerous sub-arcminute, high y structures in SZ maps. Higher resolution reveals more such structures. Increasing in the number of these objects increases the amplitude of the power spectrum while making the power spectrum flatter around the peak. The first effect is obvious and the second one can be explained by the Press-Schechter picture. The SZ power spectrum is dominated by the halo gas pressure profile $f_P(r)$ at all interesting angular scales (Komatsu & Kitayama 1999). For a singular isothermal sphere (SIS), $f_P(r) = n_e(r) k_B T(r) \propto n_e(r) \propto r^{-2}$. Its projection along the line of sight then has a θ^{-1} radial dependence, which produces an angular auto correlation function of shape $\ln(\theta)$. So the resulting power spectrum is nearly flat. A more accurate way to see the flatness behavior is to adopt the Limber's equation. The 3D gas pressure power spectrum $P_p(k) \propto \delta_p^2(k) \propto k^{-2}$, where $\delta_p(k)$ is the Fourier transform of the gas pressure profile $f_p(r)$. From Limber's equation, $C_l \propto \int P_p(l/\chi(z), z) f(z) d\chi \propto l^{-2}$, thus $l(l+1)C_l/(2\pi) \propto l^0$. Here, $f(z)$ is the redshift dependence of the SZ effect. The halo mass function also plays a role for the flat power spectrum. Since SIS profile does not apply to the core of halos, a given cluster is no longer SIS at scales smaller than its core size. Smaller clusters take over and extend the flat power spectrum.

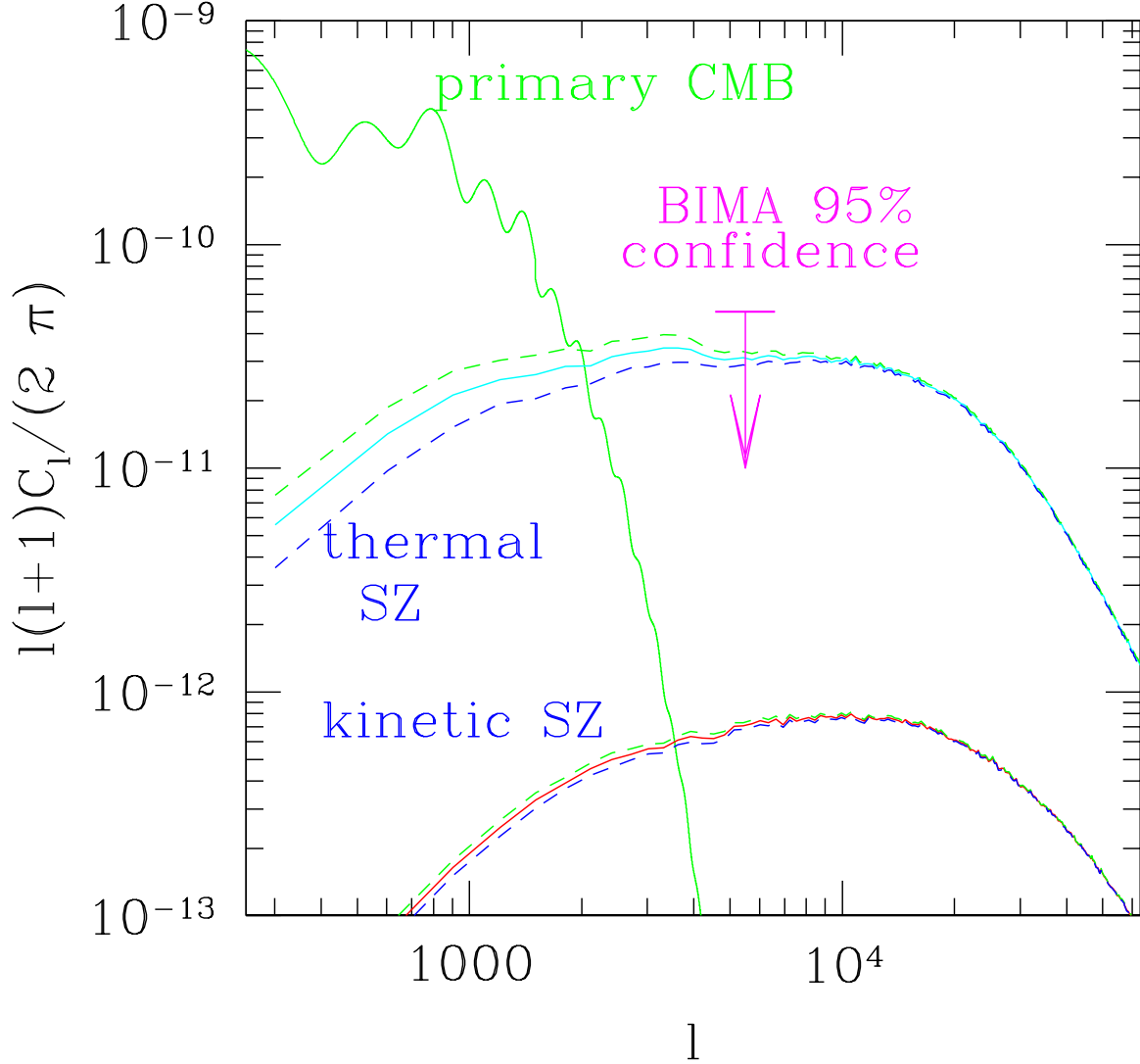


Fig. 4.— The thermal and kinetic SZ effect power spectra in our simulation. They are averaged over 40 maps. Dash lines are the corresponding 1σ upper limit and lower limit of the mean power spectrum, respectively. Both effects peak at $l \sim 10^4$. For the thermal SZ effect, the power spectrum is almost flat in the range of $2000 \lesssim l \lesssim 15000$. As a comparison, we show the BIMA result (Dawson et al. 2001) under Gaussian assumption. The comparable amplitude between theory and observation puts strict constrain on the understanding of the SZ effect.

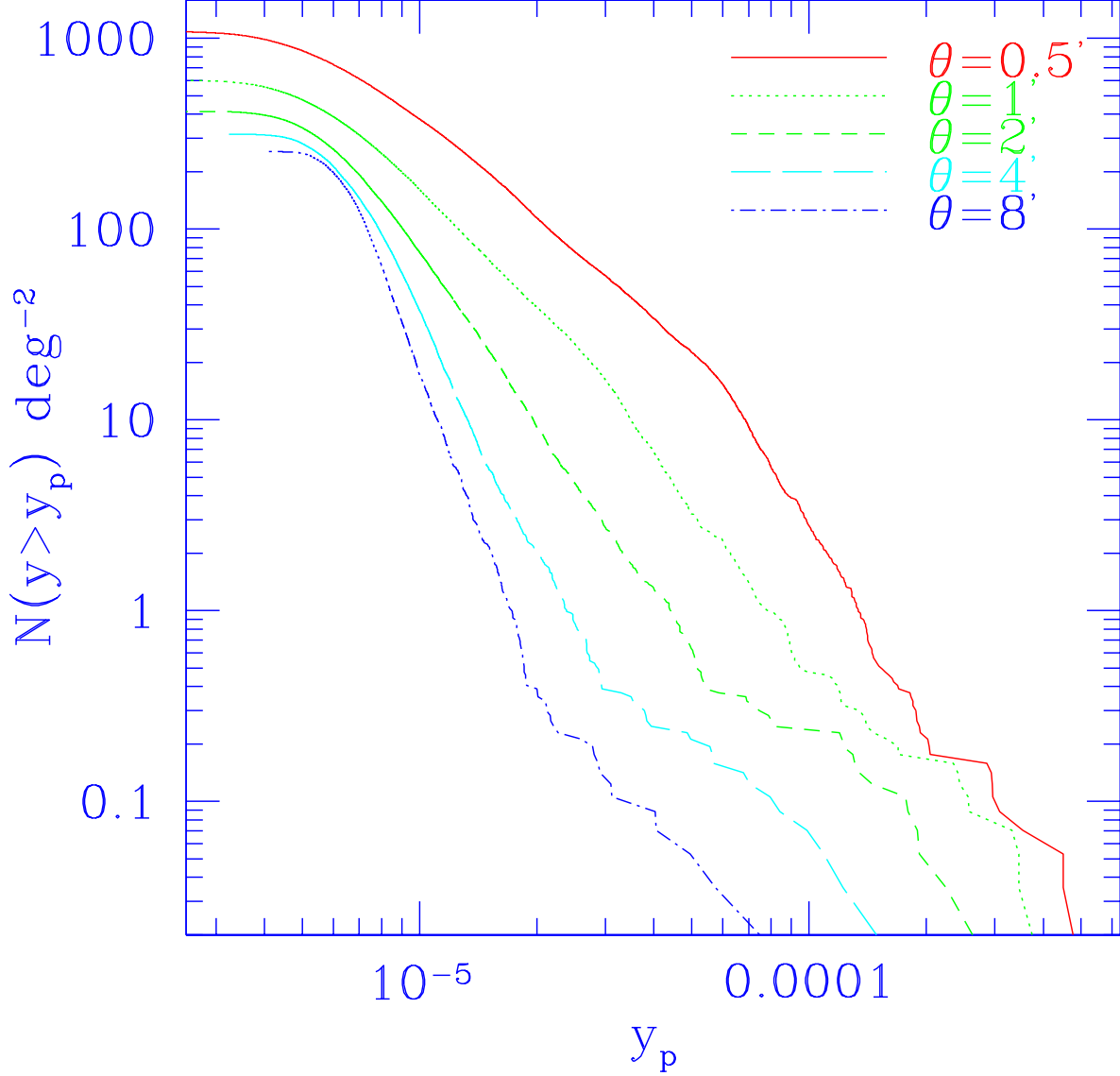


Fig. 5.— $N(y > y_p) \equiv \int_{y_p}^{\infty} \rho(y) dy$ is the number of peaks with Compton parameter y bigger than y_p . The result is averaged over 40 maps. The smoothing function we adopt is the top hat window function with radius θ . $N(y > y_p)$ as a function of θ is a direct measurement of number of structures with scale larger than θ . The quick drop of $N_{y > y_p}$ from $\theta = 0.5'$ to $\theta = 1'$ shows that there are a lot of arcminute scale structures. We believe that these structures with large y is responsible for the divergence of SZ simulations towards high resolution.

The power spectrum in our simulation clearly shows this flatness and suggests the role of these sub-arcminute halos. These halos also explain the discrepancy between our simulation and analytical predictions. $1'$ corresponds to the comoving size $\lesssim 0.8h^{-1}$ Mpc for $z < 1$ where the dominant SZ contribution comes from. This physical size corresponds to groups of galaxies. Current predictions from the Press-Schechter picture assume a lower mass limit cutoff corresponding to the mass scale of groups. In the hierarchical method, the gas window function is a free parameter, which has an implicit dependence on this lower mass cutoff (they can be related by the gas density dispersion). The cut off for contributions from groups of galaxies in analytical models results in a smaller \bar{y} and power spectrum.

If only gravitational heating is included, high mass halos and low mass halos should have comparable gas fractions. The Press-Schechter formalism predicts many more halos towards the low mass end, so one expects pure gravity simulations to have increasing power spectra with increasing high resolution. Non-gravitational heating avoids such a divergence. As described in the halo model of Pen (1999), non-gravitational heating has two effects. Firstly, the energy injection makes the halo gas less clumpy. Then the contribution to the power spectrum at smaller angular scales decreases relative to larger angular scales. This could explain the slightly differences between our simulation, CBI and BIMA results. Secondly, the non-gravitational energy injection increases the thermal energy of the gas. For halos with mass lower than some threshold, the gravity can not hold gas and most of the gas is ejected from these halos, as must have been the case for galactic size halos. This provide a reasonable lower mass limit cut off in the Press-Schechter picture. Thus the amplitude and shape of the SZ power spectrum is a sensitive measurement of the non-gravitational energy injection. To obtain a better understanding of the SZ effect, other physical processes such as radiative cooling need to be considered. Since radiative cooling through thermal bremsstrahlung is a ρ^2 process, it becomes relevant only at scales $\lesssim 100$ kpc, which corresponds to $l \gg 10^4$. These angular scales are not observable by any planed experiments, so we neglect the discussion of radiative cooling in this paper. Our current simulation has reached the resolution needed to see the contribution from small halos and the predicted SZ amplitude is already near the observed values. We expected to be able to observe the effects of non-gravitational heating from galaxy winds and other sources in the upcoming experiments.

In order to solve the discrepancy problem completely, differences between codes must be considered. Our group is currently running different codes with identical initial condition, identical cosmological parameters and various resolutions from 64^3 to 512^3 (Codes Comparison Program 2002).

Our prediction is consistent with the BIMA 95% confidence result. But the comparison between observations and theoretical predictions needs further investigation. On the simulation part, as we discuss above, the detailed normalization depends on σ_8 , non-gravitational heating and resolution effects. Observations will put strong constrains on these aspects. On the observational part, the BIMA result needs to be reconsidered. It covers the sky where no strong SZ temperature distortion due to known galaxy clusters exists. Since clusters contribute a significant if not dominant fraction

to the SZ power spectrum, the BIMA result may be smaller than the statistical mean value. Furthermore, the error of the BIMA result is estimated under the Gaussian assumption, but as we will see below, the SZ effect is highly non-Gaussian around the BIMA central multipole $l = 5530$. The strong non-Gaussianity increases the intrinsic error of the SZ power spectrum measurement. According to fig. 6, the error in the power spectrum measurement caused by the SZ effect is about 3 times larger than the corresponding Gaussian case.

Nonetheless, these results demonstrate the convergence between theory and observation. In the near future, routine and accurate measurement of the SZ effect will be possible in random fields. It will put stronger requirement for our theoretical understanding of the SZ effect and allows us to study the effects of non-gravitational heating, radiative cooling and the thermal history of the IGM.

3.2. The SZ non-Gaussianity

In contrast to the primary CMB, the SZ effect is non-Gaussian, arising from the non-linearity of the intervening gas. This non-Gaussianity affects the error analysis and may help to separate the SZ effect from the primary CMB in observation. To quantify these effects, we smooth SZ maps using a top hat window of radius θ and measure the kurtosis of the smoothed y . The kurtosis $\Theta_4 \equiv \frac{\langle y - \bar{y} \rangle^4}{\sigma_y^4} - 3$ is generally a function of smoothing scale. For a Gaussian signal, $\Theta_4 = 0$. Fig. 6 shows that $\Theta_4 \simeq 200$ at small scales as $\theta \rightarrow 0$. This result is consistent with the prediction from our hierarchical model approach of the SZ effect (Zhang & Pen 2001). We predicted, at small angular scales, $\Theta_4 \sim S_4 \sigma_g^2(z \sim 1) \sim 200$. Here, $S_4 \equiv \frac{\langle \delta^4 \rangle}{\langle \delta^2 \rangle^3} \sim 40$ is a hierarchical model coefficient (Scoccimarro & Frieman 1999) and $\sigma_g(z \sim 1) \sim 5$ is the gas density dispersion at $z \sim 1$. At large angular scales $\theta \sim 20'$, $\Theta_4 \gg 1$ and reflects the strong non-Gaussianity at this scale. It means that, at this angular scale, the dominant contribution to the y parameter is from highly non-linear regions and there is still strong correlation at angular scales down to $l \sim 1000$, as can be seen from the SZ power spectrum.

The kurtosis in multipole space $a_4 \equiv \langle |a|^4 \rangle / \langle |a|^2 \rangle^2 - 3$. As usual, $a \equiv a_{lm}$ defined by $\Theta(\hat{n}) \equiv \sum_{lm} a_{lm} Y_l^m(\hat{n})$ are multipole modes of Θ and $C_l \equiv \sum_{-l}^l |a_{lm}|^2 / (2l + 1) \equiv \langle |a|^2 \rangle$. Here, Y_l^m are the spherical harmonics. $\langle \dots \rangle$ is averaged over all $m = -l, \dots, l$ and all maps. We calculate a_4 indirectly through the map-map variance $\sigma_M(l)$ of C_l , which is related to a_4 by $\sigma_M(l) = C_l \sqrt{(a_4 + 2) / [(2l + 1) \Delta l f_{\text{map}}]}$. f_{map} is the fractional sky coverage of each map which reflects the cosmic variance and $\Delta l = 2\pi / \theta_{\text{map}}$ is the l bin size in our grid map with $\Theta_{\text{map}} = 1.19^\circ$. The factor $2l + 1$ arises because C_l is averaged over $2l + 1$ independent a_{lm} modes. In our calculation, C_l of each map is obtained using FFT under the flat sky approximation. Then we obtain the map-map variance $\sigma_M(l)$. One might expect a_4 to have similar behavior as Θ_4 at corresponding scales, for example, at small angular scales (large l), $a_4 \gg 2$. But fig. 6 shows the opposite. $a_4 \sim 50$ around $l \sim 1000$, rises slowly until $l \sim 3000$ and approaches Gaussian ($a_4 = 0$) quickly after that. In fact, Θ_4 and a_4 cannot be directly compared. The multipole modes are non-local,

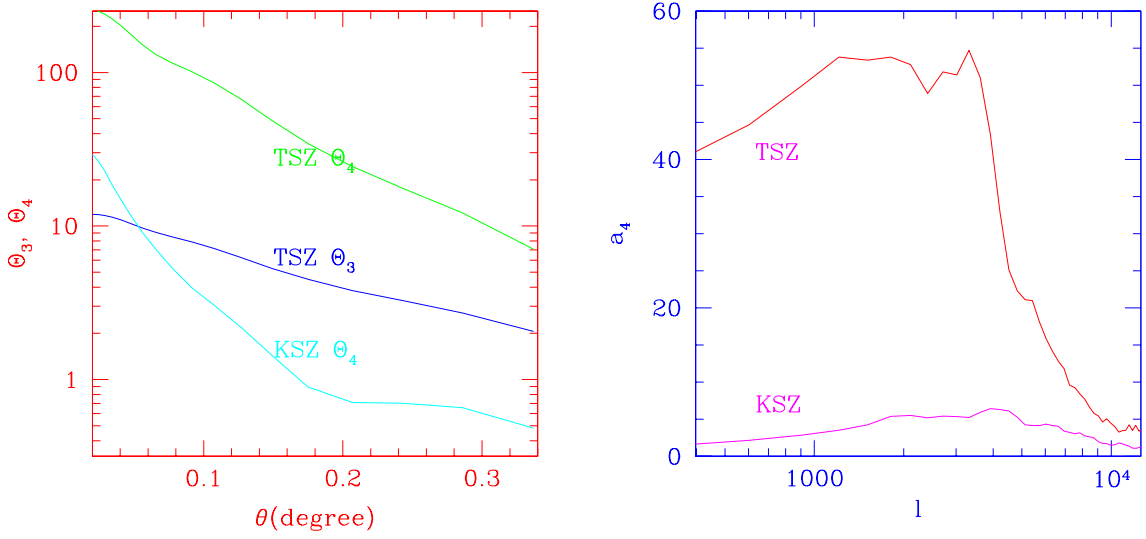


Fig. 6.— The non-Gaussianity of the SZ effects in real space (left panel) and multipole space (right panel). In real space, we measure the skewness Θ_3 and kurtosis Θ_4 . For symmetrically distributed signals, $\Theta_3 = 0$, as in the kinetic SZ case. For a Gaussian signal, $\Theta_4 = 0$. The left panel shows that the thermal SZ effect is highly non-Gaussian even to the angular size $\theta \sim 0.3^\circ$. The kinetic SZ is mildly non-Gaussian and approaches Gaussian soon towards large angular scales. The right panel shows the non-Gaussianity in multipole space. a_4 is the kurtosis in the multipole space. Because multiple modes are not local and averaged over many uncorrelated patches, the corresponding non-Gaussianity is much smaller than in the real space.

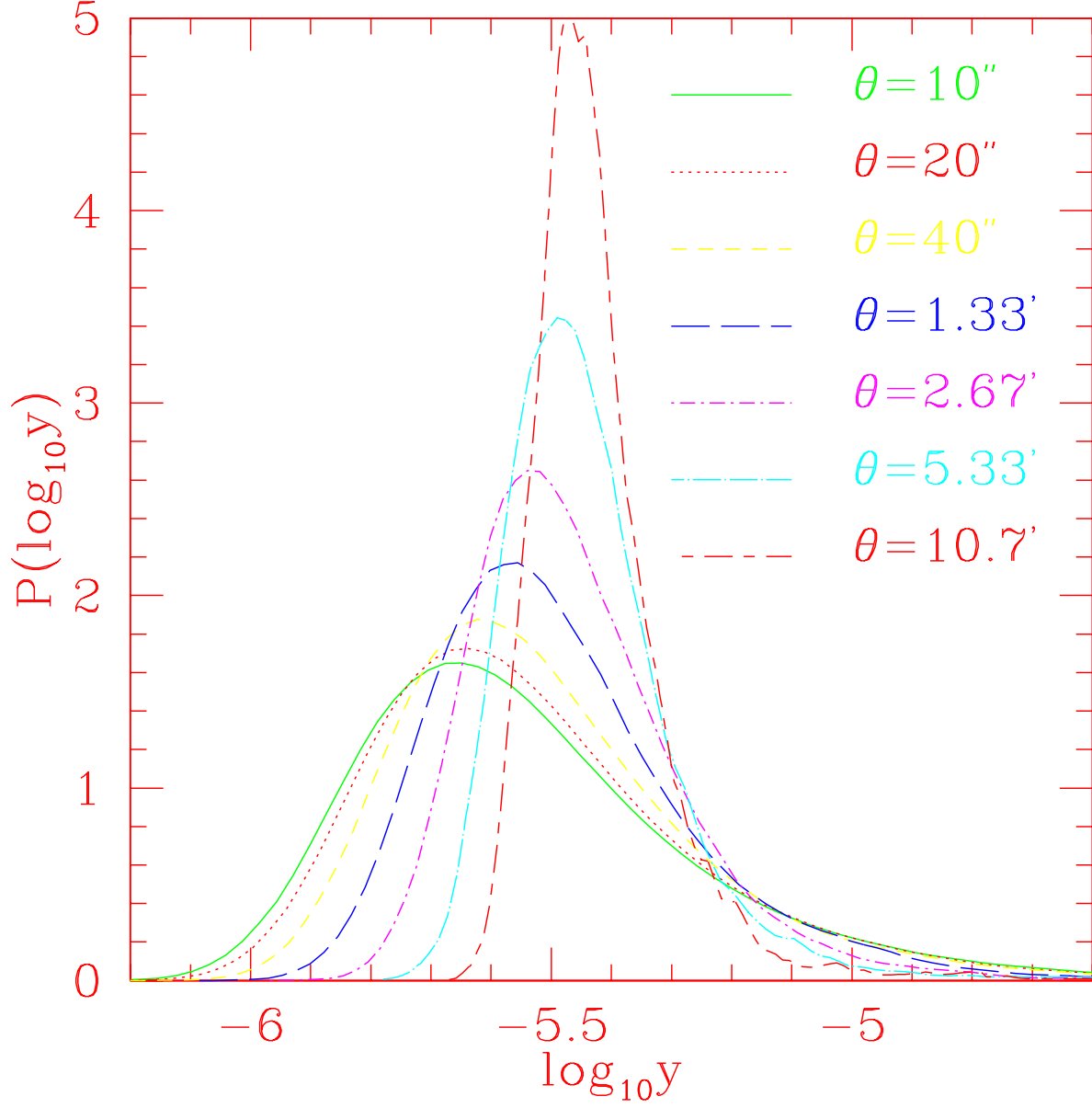


Fig. 7.— The $\log_{10} y$ PDF $P(\log_{10} y)$. We use the top hat window with radius θ to smooth the SZ map. $P(\log_{10} y)$ is roughly Gaussian. So the y PDF $P(y) = P(\log_{10} y)/(y \ln 10)$ is non-Gaussian even with a large smoothing scale as shown in fig. 6.

and averaged over many patches. If these patches are spatially uncorrelated, then the central limit theorem assures the multipole modes to be Gaussian independent of the actual non-Gaussianity of the patches. From this viewpoint, we can estimate the relation between a_4 and Θ_4 . $Y_l^m(\hat{n})$ are quickly fluctuating functions with period $\Delta\theta \simeq 2\pi/l$. Two signals separated by a distance larger than $4\Delta\theta$ will have effectively no correlation. So, for a l mode, a_{lm} is approximately the sum of $N \sim \theta_{\text{map}}^2/(4\Delta\theta)^2$ uncorrelated patches. The non-Gaussianity of each patch is roughly characterized by Θ_4 . Then, $a_4 \sim \Theta_4/N$, which may explain the behavior of a_4 .

The shape of $a_4(l)$ is similar to the shape of the pressure bias $b_p(k, z)$ (fig. 2, Zhang & Pen (2001)) defined by $b_p^2(k, z) \equiv P_P(k, z)/P_\delta(k, z)$ where P_p and P_δ are the corresponding gas pressure power spectrum and dark matter density power spectrum. This similarity suggests a common origin. In the hierarchical approach, $a_4(l)$ is related to $b_p^2(k, z)$ and we expect $a_4(l)$ to keep the similar shape but with smaller amplitude variation than b_p^2 , as illustrated by the behavior of $a_4(l)$ in our simulation and $b_p^2(k, z)$ in our analytical model.

We further show the y PDF (fig. 7) as a function of smoothing scale. The distribution of $\log_{10} y$ is roughly Gaussian, especially for large smoothing scales, as suggested by Seljak, Burwell & Pen (2001). This behavior reflects the non-Gaussianity of the y parameter, up to angular scales $\sim 10'$. The distribution of y is asymmetric since the distribution of $\log_{10} y$ is nearly symmetric. We quantify it by the skewness $\Theta_3 \equiv \langle (y - \bar{y})^3 \rangle / \sigma_y^3$ as a function of smoothing scale. For symmetric y distribution, $\Theta_3 = 0$. Fig. 6 shows that $\Theta_3 \simeq 10$ when $\theta \rightarrow 0$. This result again agrees with our hierarchical method prediction. We predicted, at small angular scales, $\Theta_3 \sim S_3 \sigma_g^{0.5} (z \sim 1) \sim 10$ where $S_3 \equiv \frac{\langle \delta^3 \rangle}{\langle \delta^2 \rangle^2} \sim 5$ (Scoccimarro & Frieman 1999). The positive sign of Θ_3 reflects the numerousness of high y regions, as suggested in fig. 5.

The kinetic SZ effect is determined by the gas momentum along lines of sight. The fractional temperature change $\Theta(\hat{n}) = -\sigma_T \int_0^{l_{\text{re}}} n_e(l\hat{n}) \frac{\mathbf{v} \cdot \hat{n}}{c} dl$. Since the direction of the gas velocity \mathbf{v} is random, we would expect $\Theta_3 = 0$ for a sufficiently large sky. The contribution from non-linear structures is partly cancelled out and thus we expect mildly non-Gaussianity. As shown in fig. (6), the kinetic SZ Θ_4 and a_4 are significantly smaller than the corresponding thermal SZ Θ_4 and a_4 (fig. 6). The kinetic SZ effect is nearly Gaussian at angular scales $\sim 20'$.

4. Simulated observations of the SZ effect

In real SZ observations, instrumental noise and primary CMB cause additional errors in the SZ statistics such as the power spectrum and peak number counts. We need to estimate these effects to derive optimal observing strategies to measure these statistics in the presence of noise. With these observational errors, our methods (§2) to extract 3D gas information is limited and we must check their feasibility. In this section, we take AMIBA as our target to address these issues.

4.1. AMIBA

AMIBA is a 19 element interferometer with 1.2 meter dishes. All dishes are closely packed in three concentric rings. It operates at $\nu_{\text{center}} = 90$ GHz with $\Delta\nu = 16$ GHz, system noise $T_{\text{sys}} = 100$ K and system efficiency $\eta \sim 0.7$. At this frequency, $\Theta \simeq -1.6y$ with $S_T(90\text{GHz}) \simeq 0.8$. The goal of this experiment is to image maps of the CMB sky with arc minute resolution. We consider observations with fixed integration time and aim at finding the optimal sky area Ω and sky fractional coverage $f_{\text{sky}} = \Omega/4\pi$ for a given statistics.

For closely packed interferometers observing such weak signals, the ground fringe can be a major source of noise. To eliminate the ground fringe, AMIBA plans to drift scan: the telescope is parked while the sky drifts by. This assures that the ground fringe remains constant with time. The mean value of each fringe is then subtracted from the scan, cleanly eliminating the ground. A field is mosaicked by a series of adjacent scans, and the most uniform coverage is achieved by incrementally offsetting the pointing center on each scan to yield a finely sampled 2-D map. The raw output of the experiment are correlations, two for each baseline, polarization and frequency channel, corresponding to the real and imaginary correlator outputs. We can think of each of these outputs to correspond to an image of the sky filtered through some anisotropic beam. As a first step, we can combine degenerate baselines and polarizations, reducing the 171 baselines to 30 non-degenerate baselines. Since the CMB is expected to not be significantly unpolarized, we can combine the two polarization channels, leading to 60 raw maps per frequency channel. These maps can be merged optimally into one global map by convolving each map with its own beam, and scaling each map to the same noise level, and coadding these maps, resulting in a 'clean' map. Each of the constituent maps had explicitly white noise, so the noise statistics of the summed map are easily computable. The 'clean' map can be deconvolved by the natural beam, resulting in a 'natural' map. This 'natural' map is an image of the sky convolved with the natural beam of the telescope plus white noise. The angle averaged natural beam is shown in fig. 9. The CMB intensity fluctuation δI_ν measured by AMIBA has three components: the primary CMB, the SZ effect and the instrumental noise. It is related to the temperature fluctuation by

$$\frac{\delta I_\nu}{I_\nu^{\text{CMB}}} = \frac{x \exp(x)}{\exp(x) - 1} \left[\left(\frac{\delta T}{T} \right)_{\text{CMB}} + \left(\frac{\delta T}{T} \right)_{\text{SZ}} + \frac{\delta T^N}{T_{\text{RJ}}} \right] \quad (6)$$

Here, $(\frac{\delta T}{T})_{\text{CMB}}$ and $(\frac{\delta T}{T})_{\text{SZ}}$ are the corresponding temperature fluctuations seen through the AMIBA natural beam. $x = h\nu/k_B T_{\text{CMB}}$. We have chosen the normalization of the beam such that the noise power spectrum is white with

$$C_N = 4\pi T_{\text{sys}}^2 f_{\text{sky}} / (2\Delta\nu t \eta^2) / T_{\text{RJ}}^2. \quad (7)$$

$T_{\text{RJ}} = T_{\text{CMB}} x^2 \exp(x) / [\exp(x) - 1] = 2.22$ K is the Raleigh-Jeans equivalent CMB temperature at $\nu = 90$ GHz. The factor of 2 is due to the two polarizations of the AMIBA experiment. For a single dish of infinite aperture, with a single pixel detector, the window would be identically one: the scanned image is just the CMB distribution on the sky. Since AMIBA has many detectors,

one can combine them to either lower the noise, or to boost the signal. We have chosen to use the equivalent noise of a single pixel single dish experiment, and normalized the beam accordingly. We calculate the natural beam $W_N(l)$ by equation (17) and (46) of Pen et al. (2002). The natural beam in multipole space and real space are shown in fig. 9. The natural beam has a FWHM of $2'$. It peaks at $l_i \simeq 2\pi\lambda/D_i$. Here, $\lambda \simeq 3.3$ mm is the AMIBA operating wavelength and D_i is the distance of the i th baselines. The first peak $l_1^{\text{peak}} \sim 2273$ corresponds to the shortest base line $D_1 = 1.2$ m. At this angular scale, the sum of all the baselines improves throughput by a factor of almost three ($\epsilon \simeq 2.77$). This is analogous to having a nine pixel detector on a single dish. More detailed definitions of the beams and strategies are described in detail in (Pen et al. 2002).

In our simulated pipeline, we add primary CMB map fluctuations to our simulated sky maps using CMBFAST-generated (Seljak & Zaldarriaga 1996) power spectra with same cosmological parameters except for the use of COBE normalization for σ_8 , which is slightly different from our simulation value. As we will show below, the primary CMB is not the main source of noise for the SZ power spectrum measurement at AMIBA angular scales ($l > 2000$) and is negligible in SZ cluster searches. So the effect of this inconsistent σ_8 is insignificant in our analysis. Adding SZ maps and CMB maps, we obtain simulated sky maps (fig. 8). In these maps, SZ structures, especially those caused by diffuse IGM are superimposed with the primary CMB. We then convolve these maps with the natural beam. The beam function decreases quickly to zero towards large angular scales where the primary CMB dominates, so it efficiently filters most primary CMB structures larger than this scale. We then add the noise given by eqn. (7) to this map. The normalization in the beaming and filtering (described below) process is arbitrary. We choose the normalization in such a way that the power spectrum of the map at the scale of the peak response does not change after beaming or filtering. It corresponds to normalizing the global maximum of the beam function to be unity. Under such normalization, when we add instrumental noise to the simulated CMB+SZ map, the noise is depressed by a normalization factor $\epsilon \simeq 2.77$. Our 1.19° map has 2048^2 pixels, so the white instrumental noise dominates on small scales. For a 20 hours/deg² survey, the dispersion of the noise temperature fluctuation $\sigma_N = T_{\text{sys}}/\sqrt{(2\Delta\nu t_{\text{pixel}})/(\eta T_{\text{RJ}}\epsilon)} \sim 0.002 \gg \bar{y}$. t_{pixel} is the observing time for each pixel. So all signals are hidden under the instrumental noise. One needs further filtering to obtain an image that is not overwhelmed by the small scale noise. Ignoring the CMB fluctuations, we know that point sources have the shape of the beam. A point sources optimized search would convolve the natural map with the shape of the beam, and peaks in this map correspond to the maximum likelihood locations of point sources. We can think of the CMB as a further source of noise, and filter that away as well. In this case, the filter depends on the ratio of CMB and noise amplitudes, i.e. the actual integration time. One can also optimize a filter for a structure of a known intrinsic shape. Since clusters are approximately isothermal, a better filter would be one matched to the extended isothermal nature, where objects in the natural map have the shape of an isothermal sphere convolved with the natural beam. Combining all these consideration, the optimal filter for noise cleaning is given by $W_C(l) = W_F(l)W_N(l)/(1 + W_N^2 C_l^{\text{CMB}}/C_N)$ (fig. 9). $W_F(l)$ is the Fourier transform of the source intrinsic shape $W_F(\mathbf{r})$. For point sources, $W_F(l) = 1$. For clusters, on scales smaller than the cluster virial radius and larger than the core radius, $y(\theta) \propto \theta^{-1}$ (θ is

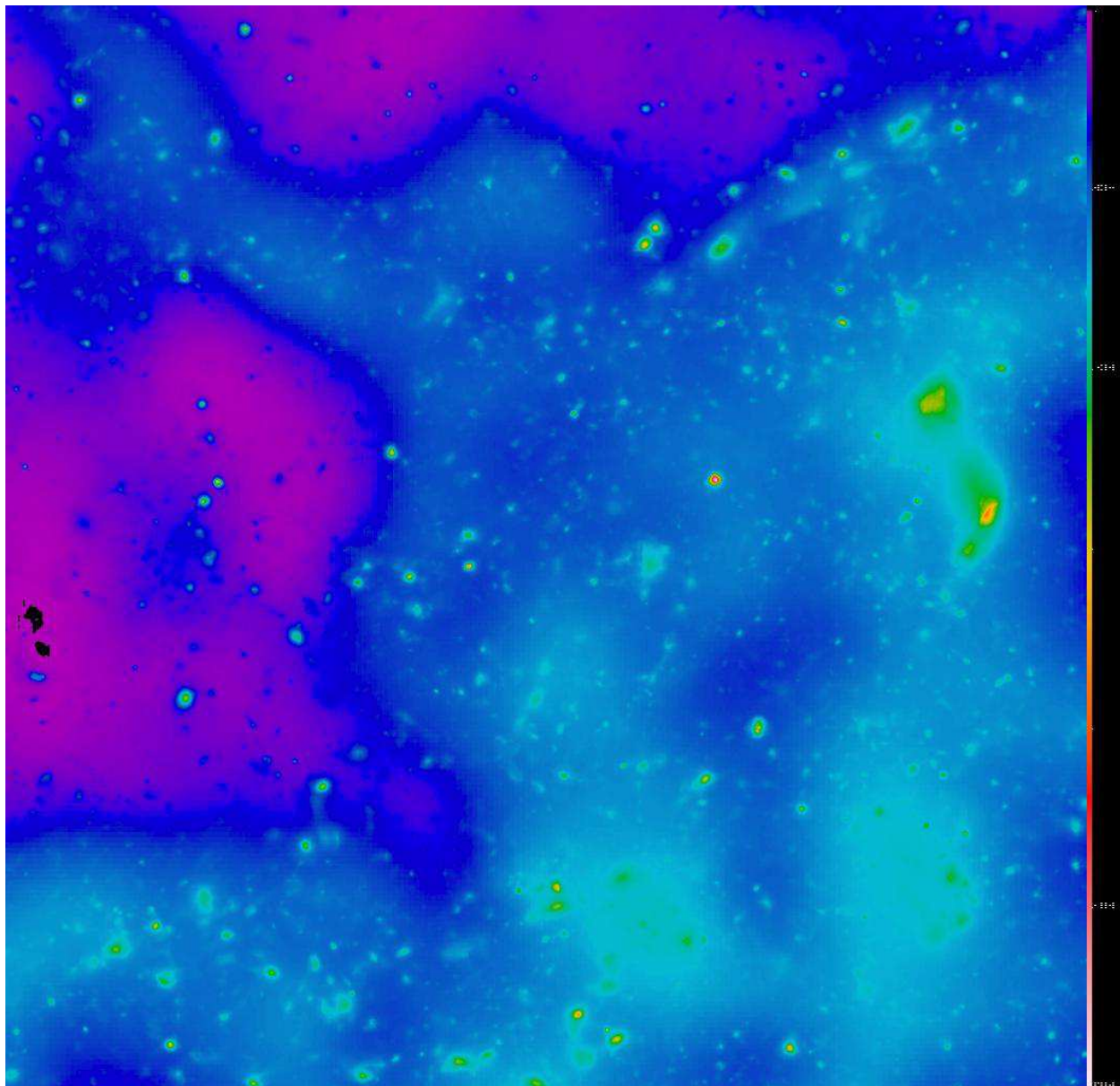


Fig. 8.— A combined SZ+CMB map. At large angular scales, the primary CMB dominates and smears the structure of the thermal SZ effect.

the angular distance to the cluster center). Then $W_F(l) \propto l^{-1}$. Since the corresponding angular size of the core radius is much smaller than the beam size, the above approximation is sufficiently accurate. We shown the filter with 280 hours per square degree scan rate in figure 9. It has a FWHM of $2'$. In multipole space, it drops to near zero at angular scales $l \sim 1500$ and $l > 9000$ and peak at cluster scales $l \sim 3000$. So it is efficient to filter away the residual primary CMB and the instrumental noise while amplifying SZ signals. We tried different sky scan rates to find the optimal survey strategy. We show final resulting maps in fig. (10) with 280 hours per square degree scan rate. With the simulations we have the luxury of seeing maps with (right panels of fig. 10) and without noise (left panels of fig. 10). We discuss the simulated AMIBA measurement of the SZ power spectrum and cluster searching in the next two subsections.

4.2. The SZ power spectrum in the simulated AMIBA experiment

One of the key goals of AMIBA is to measure the SZ power spectrum. As discussed in §3, it is a sensitive measure of the gas thermal history. Furthermore, combining the cross-correlation with photometric galaxy surveys, an SZ survey can measure the IGM pressure power spectrum as a function of redshift. This gives us access to the evolution of the IGM state. For the purpose of the SZ power spectrum estimation, the two noise sources, the primary CMB and the thermal instrument noise, are both Gaussian. The intrinsic SZ variance causes further error. The combined error for the power spectrum estimation is

$$\Delta C_l^{\text{SZ}} = \sqrt{\frac{a_4(l)C_{\text{SZ}}^2(l) + 2[C_{\text{SZ}}(l) + C_l^{\text{CMB}} + C_l^{\text{N}}/W_N^2]^2}{(2l+1)\Delta l f_{\text{sky}}}}. \quad (8)$$

If the SZ effect is Gaussian ($a_4 = 0$), we recover the usual expression of the error. We take a large bin width $\Delta l = l/4$ to estimate the error. Since the SZ power spectrum is nearly flat in the range $l \sim 2000 - 15000$, this choice of bin size does not lose significant information. At large angular scales ($l < 1500$), the error from primary CMB dominates, and at small scales ($l > 5000$), the instrumental noise dominates. In the intermediate scales, the intrinsic error of the SZ effect dominates. Different errors have different dependences on the sky coverage. Increasing f_{sky} while fixing the integration time, the errors from primary CMB and SZ effect decrease but the the one from the instrumental noise increases, so there exists a optimal sky coverage for a given integration time. Since the errors from primary CMB and SZ effect are both scale as $f_{\text{sky}}^{-1/2}$ and the instrumental noise scales as $f_{\text{sky}}^{1/2}$, the minimum error is obtained when $(a_4 + 2)C_{\text{SZ}}^2 + 2C_l^{\text{CMB}} + 4C_{\text{SZ}}C_l^{\text{CMB}} = 2C_N^2/W_N^4$, which gives the optimal sky coverage. For 1000 hours of observing, several hundred square degree sky coverage is nearly optimal (fig. 12). Fig. 11 shows that AMIBA is able to measure the SZ power spectrum with an accuracy of $\sim 40\%$ for l between 2000 and 5000 in 1000 hour observing of 100 square degrees of sky. The strong dependence of the SZ effect on σ_8 strongly affects our error estimation. A smaller σ_8 reduces the signal and S/N. In order to keep S/N, smaller sky coverage is needed to reduce the noise. The dependence of the optimal sky coverage $f_{\text{sky}}^{\text{opt}}$ on σ_8 is shown in fig. 12. In

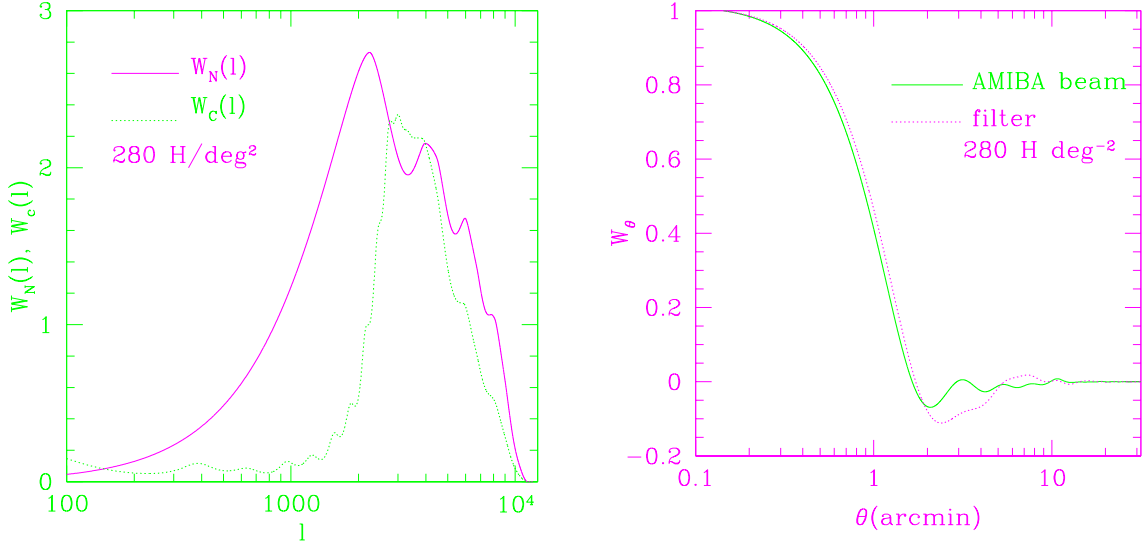


Fig. 9.— The natural beam and optimal filter functions of AMIBA in multipole (left panel) and real space (right panel). The main goal of the beaming and filtering is to filter away the primary CMB, which dominates at large scale ($l \lesssim 1000$) and instrumental noise at small scale ($l \rightarrow \infty$). This goal is clearly illustrated in the large and small l behavior of these functions. The optimal filter depends on the noise amplitude. We show the case for AMIBA scan rate 280 hours deg⁻². This filter has a $\sim 2'$ FWHM.

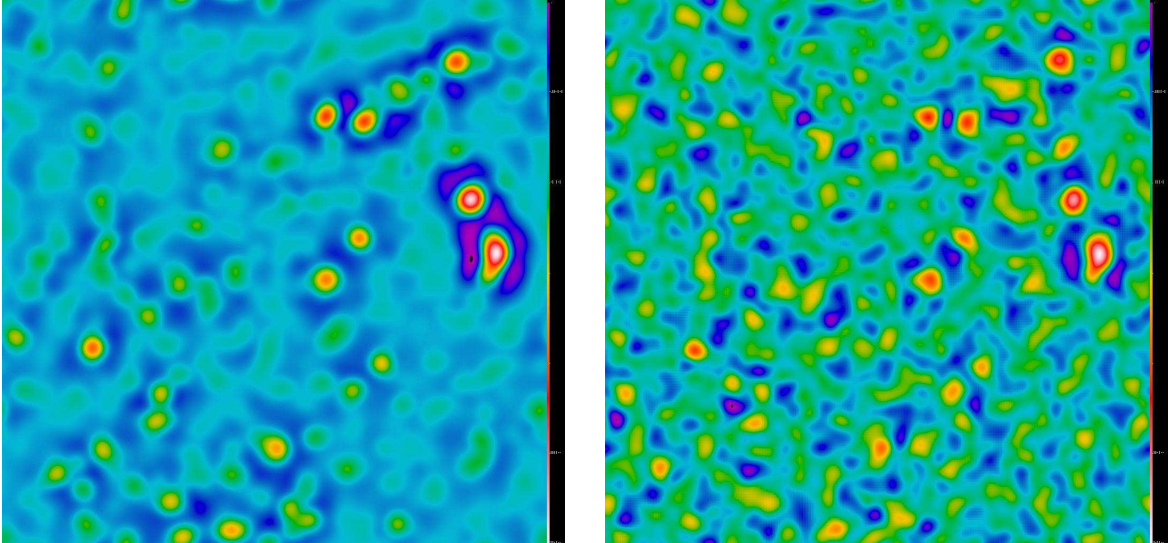


Fig. 10.— Filtered maps without noise (left panel) and with noise (right panel) of AMIBA 390 hours observing. Many peaks in the total map are not real signal peaks while some peaks in the clean map disappear in the total map. For AMIBA’s frequency, $\Theta = -1.6y$. For clarity, we plot $-\Theta$.

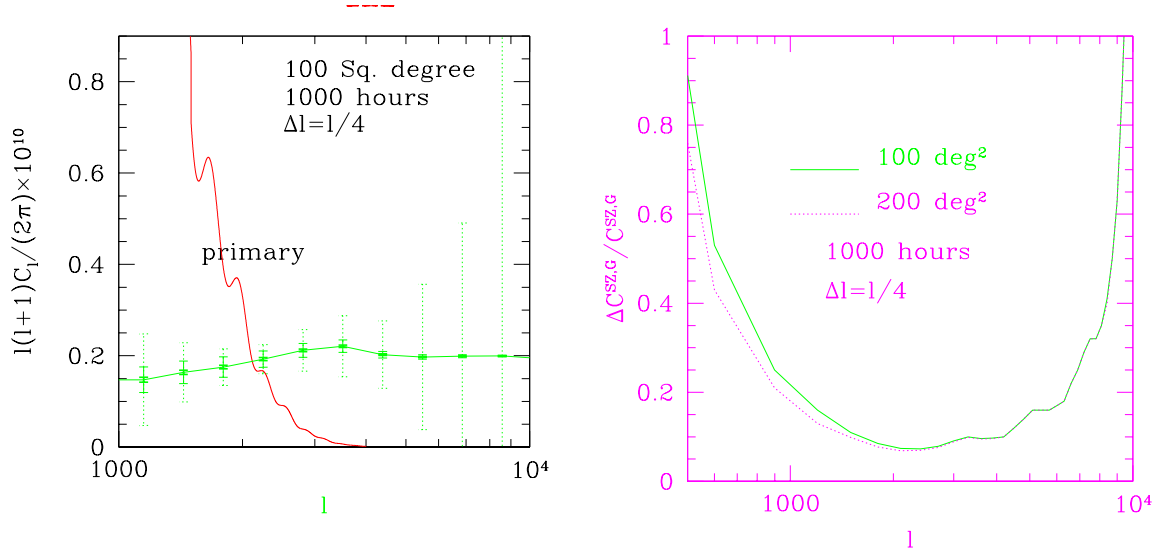


Fig. 11.— Errors in the AMIBA measurement of SZ power spectrum (left panel) and cross correlation (right panel) with SDSS galaxies. The SZ power spectrum is 0.8^2 times of the one in fig. 4 since at AMIBA operating frequency $\nu = 90$ GHz, $\Theta = -1.6y$ as contrast to $\Theta = -2y$ in the Rayleigh-Jeans regime. The thick solid error bar is the Gaussian variance, the thin solid error bar is the actual variance calculated from a 40 map ensemble and the dot error bar is the total error including primary CMB and instrumental noise. For a 1000 hours survey of a 100 deg² area, the accuracy in the SZ power spectrum measurement is about 40% at the range of $2000 < l < 5000$. In the same survey, the measured cross correlation has about 20% accuracy at similar l range.

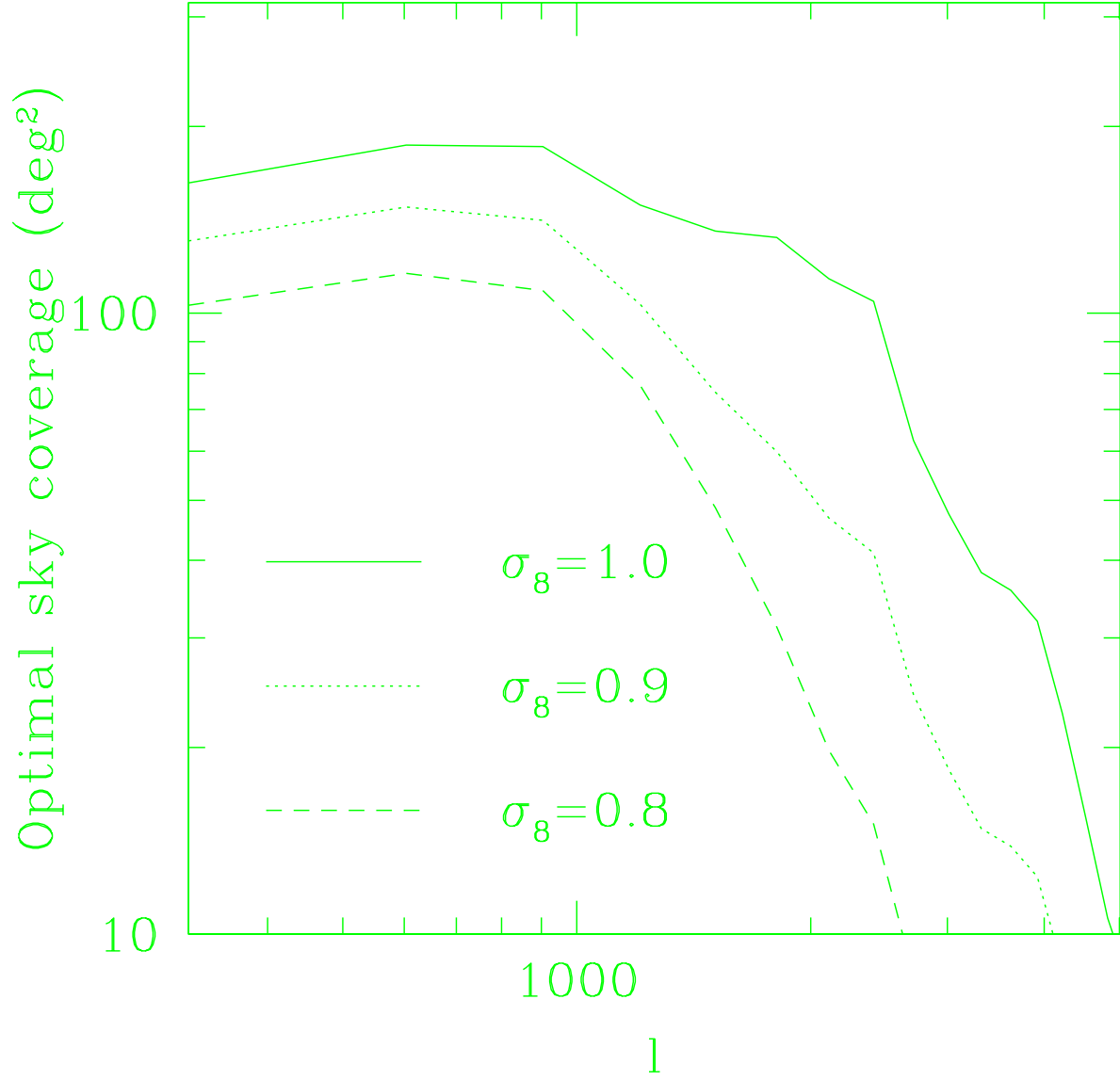


Fig. 12.— The dependence of the optimal sky coverage in the SZ power spectrum measurement on σ_8 in a 1000 hour AMIBA survey. Our simulation used $\sigma_8 = 1.0$. The $\sigma_8 = 0.9$ and $\sigma_8 = 0.8$ cases are estimated assuming the strongest dependence of C_l on σ_8 : $C_l \propto \sigma_8^9$.

this estimation, we have assumed the most extreme dependence of the SZ effect on σ_8 , namely, $C_{SZ}(l) \propto \sigma_8^9$.

If we cross correlate the observed SZ effect with SDSS, we can extract the underlying 3D gas pressure power spectrum and pressure-galaxy cross correlation. To test its feasibility, we estimate the error in the angular cross correlation measurement by

$$\frac{\Delta C^{SZ,G}(l)}{C^{SZ,G}(l)} = \sqrt{\frac{1 + r^{-2}(1 + C^{CMB}/C_{SZ} + C_{SZ}^N/C_{SZ})(1 + C_G^N/C^G)}{(2l+1)\Delta l f_{sky}}}. \quad (9)$$

SDSS will cover $f_{sky}^{SDSS} = 1/4$ of the sky and will detect $N_G \simeq 5 \times 10^7$ galaxies with photometry in five bands. The Poisson noise in SDSS has the power spectrum $C_G^N = 4\pi f_{sky}^{SDSS}/N_G$. We assume a linear bias between galaxy number overdensity and dark matter overdensity to calculate the galaxy surface density power spectrum $C^G(l)$. Since SDSS is flux limited, we take the galaxy selection function $\frac{dn}{dz} = 3z^2/2/(z_m/1.412)^3 \exp[-(1.412z/z_m)^{3/2}]$ (Baugh & Efstathiou 1993) with a SDSS fit $z_m = 0.33$ (Dodelson et al. 2001). The galaxy-SZ power spectrum $C^{SZ,G}(l)$ is estimated by the SZ-galaxy cross correlation coefficient $r \equiv C^{SZ,G}/\sqrt{C^{SZ}C^G}$. We choose $r = 0.7$ (Zhang & Pen 2001) as predicted by the hierarchical model. We show the error in fig. 11. The larger the sky coverage, the smaller the error. With the optimal scan rate for SZ power spectrum measurement, the accuracy in the cross correlation measurement is about 20%.

4.3. AMIBA cluster search

Another important goal of AMIBA is searching for clusters. In the power spectrum measurement, the observable is the direct sum of signal and noise, so the noise contribution can be subtracted linearly in the power spectrum. The only net effect is an increase in the error bars, which is important only at very small angular scales or very large scales. But when counting peaks in a map, effects of noise are much more complicated and are not easily interpreted. Noise introduces false peaks in the observed SZ maps, changes the value of real peaks, shifts the peak positions and even makes real peaks disappear. So noise affects the measurement of cluster counts, richness and positions. Thus we would want a much longer integration time for the purpose of cluster search. We count peaks in the filtered maps with and without noise and quantify these effects as follows. (1) We estimate the accuracy of y measurements by calculating the y dispersion of noise σ_y^N . (2) We distinguish real peaks from false peaks by comparing the position and amplitude of each peak in the clean SZ maps without noises and in the total maps with noises (fig. 13). One FWHM is roughly the size of noise structures after filtering and corresponds to the maximum position shift noise can exert to real peaks. $2\sigma_y^N$ is roughly the maximum peak amplitude change that noise can cause. So, if a peak in a total map whose distance to the nearest peak in the corresponding clean SZ map is less than one FWHM of the filter and its value is in the $2\sigma_y^N$ range of the real value, we classify it as real. (3) We estimate the accuracy of y peak CDF by comparing clean SZ maps, noise maps and total maps (fig. 14). For signal peaks with $y \gg \sigma_y^N$, the signal peaks remain to

be peaks in the total map. Noise mainly changes the amplitude of the i th real signal from y_i to $y_p = y_i + y^N$ in the total map. Here, y^N is the value of the noise and y_p is the value in the total map. Since noise is Gaussian, we know the distribution of y^N , which can be described by $P(y, \sigma_y^N)$, the probability for the Gaussian noise with dispersion σ_y^N to have value bigger than y . Then we can related the CDF of peaks in clean maps to the one of total maps by

$$N_{tot}(y > y_p) = \sum_i^N P(y_p - y_i, \sigma_y^N). \quad (10)$$

This relation gives a good fit in the $y \gg \sigma_y^N$ regime. For signals with $y \sim \sigma_y^N$, noise changes both y value and positions of some peaks, makes some peaks disappear and introduces a large fraction of false peaks. The sum of $N_{tot}(y > y_p)$ in eqn. (10) and $N_{noise}(y > y_p)$ considers the effect that noise introduces false peaks and we expect that it would give a good fit in the region where $y \sim 2\sigma_y^N$. We show the modelled CDF of peaks in total maps following above procedures in fig. 15. The result is well fitted in the range $y > 2\sigma_y^N$ with better than 30% accuracy.

The optimal survey should find clusters as quickly as possible and measure the y parameter and peak CDF as accurately as possible. We find that the optimal scan rate for cluster searching is about 280 hours deg^{-2} . At this rate, the rate of cluster detection is about 1 every 7 hours allowing for a false positive rate 20%. The measured cluster CDF $N(y > y_p)$ is accurate to 30% up to $N \simeq 60 \text{ deg}^{-2}$. We recall that the optimal scan rate for SZ power spectrum measurement is about 10 hours deg^{-2} . At this rate, the cluster detection rate is about 1 cluster every 60 hours. We can consider the effect of cosmology on our estimation. A smaller σ_8 reduces signals and therefore the cluster detection rate. We assume the extremest dependence of the y parameter on σ_8 , namely, $y \propto \sigma_8^3$ as predicted by Zhang & Pen (2001). For $\sigma_8 = 0.9$, the detection rate decreases by a factor of four. But the optimal scan rate remains approximately the same.

At this optimal scan rate, in a 1000 hour AMIBA survey, several hundred clusters can be found. Comparing the SZ cluster counts to Press-Schechter predictions or X-ray surveys (§2) allows us to reconstruct the thermal history of the IGM and non-gravitational heating, which is expected to arise from galaxy formation feedback (Pen 1999).

5. Conclusion

We have performed the largest high resolution SZ simulations to date, and analysed the results. We found further increases in the power spectrum relative to previous simulations, and significantly more small scale structures. This trend is confirmed in Press-Schechter estimates, and suggests nominally increasing power spectra. The small structure behavior may not be a robust prediction, since non-gravitational effects will significantly modify those scales. We have examined the skewness and kurtosis on the sky maps, found a strong non-Gaussianity on subdegree scales and confirmed the log-normal distribution found in previous studies. The Gaussian estimates of power spectrum

sample variances are less severely affected, due to the averaging of many patches by each Fourier modes. But its effect on the power spectrum error analysis is significant.

We simulated SZ observations with AMIBA, and analyzed the sensitivity for different scan rates. In a 1000 hour survey, the optimal strategy for power spectrum estimations is to scan several hundred square degrees. The SZ angular power spectrum measured in such survey can be determined to an accuracy of $\sim 40\%$ over a range of $2000 \lesssim l \lesssim 5000$. A cross correlation with SDSS should allow an accuracy of 20% in the cross correlation measurement, which suggests that the time resolved measurement of the pressure power spectrum is then possible. This scan rate results in a low detection rate of clusters of galaxies, approximately one per 60 hours with a false positive rate of 20%. For the purpose of cluster search, the optimal scan rate is around 280 hours per square degree, which could find 1 cluster every 7 hours, with the accuracy of 30% in the cluster y measurement and 30% in the cluster CDF up to $N(y > y_p) \sim 60 \text{ deg}^{-2}$.

The predicted SZ power spectrum is consistent with recent indications from the CBI experiment (Mason et al. 2001; Sievers et al. 2001) and the BIMA upper limit (95% confidence). But it is higher than the BIMA $1\text{-}\sigma$ result. This may be a first indication of IGM non-gravitational feedback. Future blank sky surveys with data analysis considering actual SZ non-Gaussianity will provide us with a quantitative understanding of the thermal history of the universe.

Acknowledgments: We thank Uros Seljak for the code to generate 2D SZ maps and lots of helpful suggestions. We thank Josh Frieman, Scott Dodelson and Albert Stebbins for the discussion of SDSS.

REFERENCES

- Array for Microwave Background Anisotropy, 2003, <http://www.asiaa.sinica.edu.tw/amiba/>
- Atrio-Barandela, F. & Mucket, J., 1999, ApJ, 515, 465
- Barbosa, D., Bartlett, J.G., Blanchard, A. & Oukbir, J., 1996, A&A, 314, 13
- Baugh, C.M. & Efstathiou, G., 1993, MNRAS, 265, 145
- Church, S.E., et al., ApJ, 484, 523
- Dubinski, J., TreeSPH; Ruetalo, M. & , Gasoline code; Woo, T. & Wu, J., Gadget code; Zhang, P. & Pen, U., MMH code; 2002, in preparation.
- Cole, S. & Kaiser, N., 1988, MNRAS, 233, 637
- Cooray, A., 2000, Phys. Rev. D, 62, 103506
- Cooray, A., Hu, W. & Tegmark, M., 2000, ApJ, 540, 1

- da Silva, A., et al. 2000, MNRAS, 317, 37
- Dawson, K.S., et al. 2001, ApJ, 553, L1
- Dodelson, S., et al. 2001, astro-ph/0107421
- Fox, D. & Pen, U.L., 2001, astro-ph/0110311
- Fukugita, M., Hogan, C.J. & Peebles, P.J.E., 1998, ApJ, 503, 518
- Fixsen, D.J., et al. 1996, ApJ, 473, 576
- Holzapfel, W.L., et al. 2000, ApJ, 539, 57
- Komatsu, E. & Kitayama, T., 1999, ApJ, 526, L1
- Makino, N., & Suto, Y., 1993, ApJ, 405, 1
- Mason, B., CBI Collaboration, 2001, BAAS, 199, 3401
- Mason, B.S., Myers, S.T. & Readhead, A.C.S., 2001, ApJ, 555, L11
- Molnar, S. & Birkinshaw, 2000, ApJ, 537, 542
- Netterfield, B., et al. 2001, astro-ph/0104460, submitted to ApJ.
- Partridge, R.B., et al., 1997, ApJ, 483, 38
- Pen, U.L., 1998a, ApJS, 115, 19
- Pen, U.L., 1998b, ApJ, 498, 60
- Pen, U.L., 1999, ApJ, 510, L1
- Pen, U.L., et al., 2002, <http://www.cita.utoronto.ca/~pen/download/Amiba/>
- Perna, R. & Loeb, A., 1998, ApJ, 503, L135
- Persic, M. & Salucci, P., 1992, MNRAS, 258, 14P
- Press, W.H. & Schechter, P., 1974, ApJ, 187, 425
- Pryke, C., et al. 2001, astro-ph/0104490, submitted to ApJ.
- Refreigier, A. et al., 2000, Phys. Rev. D, 61, 123001
- Scaramella, R., Cen, R. & Ostriker, J., 1993, ApJ, 416, 399
- Schechter, P., 1976, ApJ, 203, 297
- Scoccimarro, R. & Frieman, J., 1999, ApJ, 520, 35

- Seljak, U. & Zaldarriaga, M., 1996, ApJ, 469, 437
- Seljak, U., Burwell, J. & Pen, U., 2001, Phys. Rev. D, 63, 063001
- Silk, J. & White, S., 1978, ApJ, 226, L103
- Sievers, J., et al. 2001, BAAS, 199, 3402
- Sloan Digital Sky Survey, 2002, <http://www.sdss.org/>
- Springel, V., White, M. & Hernquist, L., 2001, ApJ, 549, 681
- Subrahmanyam, R., et al., 2000, MNRAS, 315, 808
- Weller, J., Battye, R. & Kneissl, R., 2001, astro-ph/0110353
- Zel’dovich, Y.B. and Sunyaev, R., 1969, Ap&SS, 4, 301
- Zhang, P.J. & Pen, U.L., 2001, ApJ, 549, 18
- Zhang, P.J., Pen, U.L. & Seljak, U., 2002, in preparation.

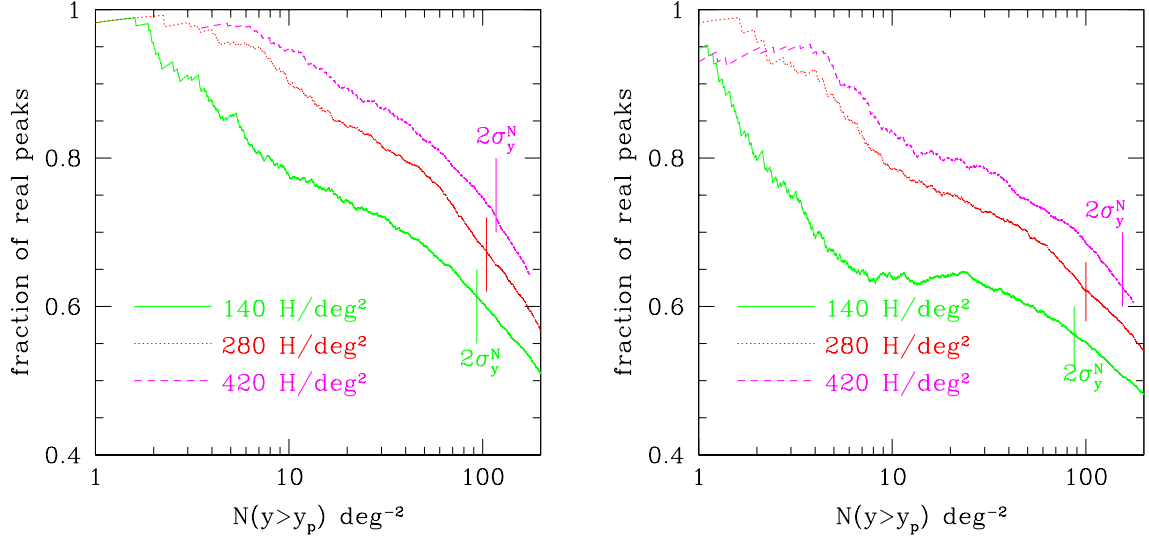


Fig. 13.— The fraction of real peaks as a function of number of peaks in simulated AMIBA observing (left panel) with $\sigma_8 = 1.0$ and the expected result scaled for a different $\sigma_8 = 0.9$ (right panel). In our simulation, the optimal cluster searching rate is ~ 1 cluster every 7 hours, which drops to ~ 1 cluster every 30 hours for $\sigma_8 = 0.9$. We have assumed the extremest y dependence on σ_8 : $y \propto \sigma_8^3$.

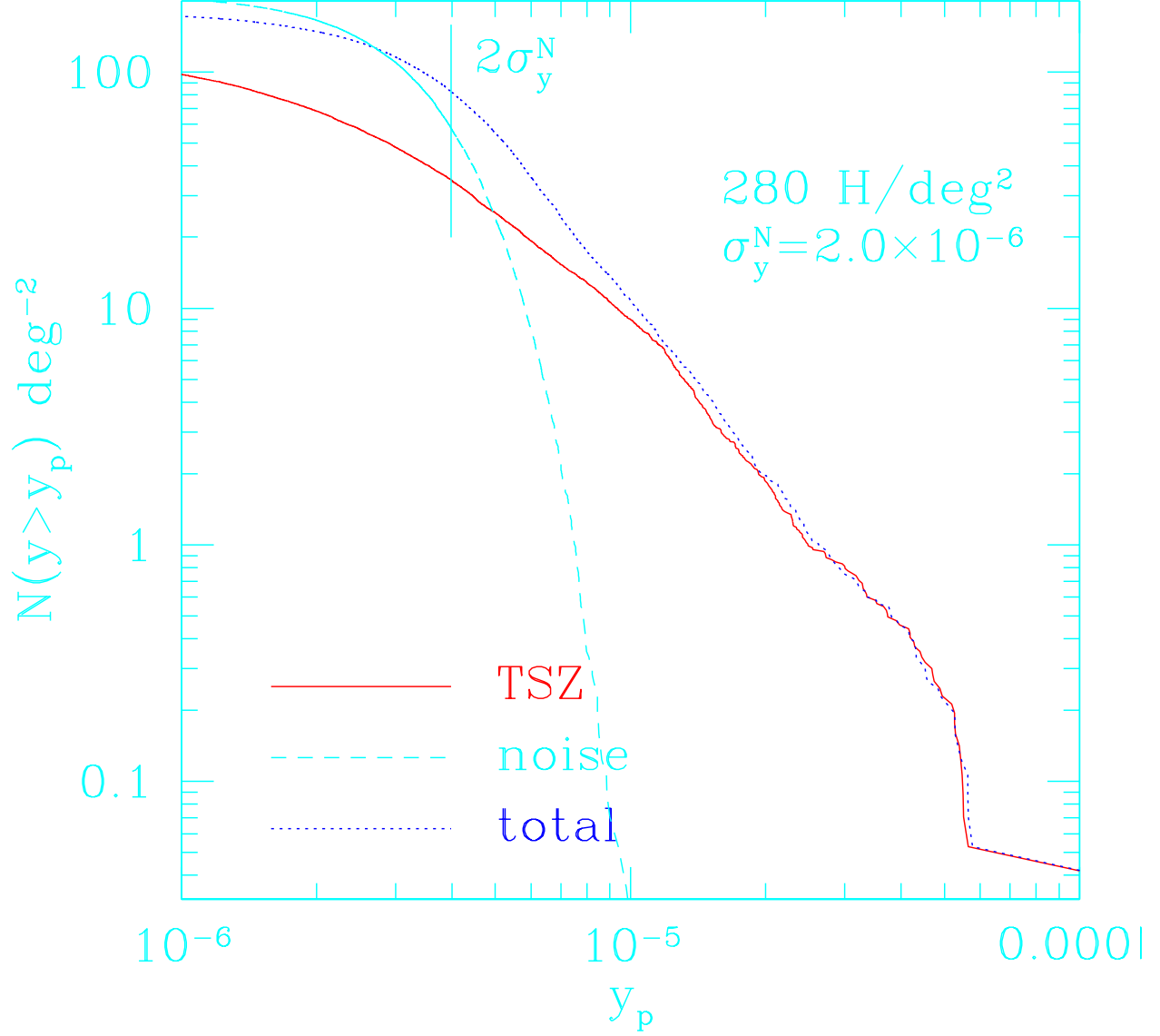


Fig. 14.— Peak distribution $N(y > y_p)$ in simulated AMIBA observing. All results are averaged from 40 maps. the 'TSZ' line is the pure SZ peak distribution without noise and the 'total' line is what would be measured in our simulated AMIBA experiment. We see that when $y < 2\sigma_y^N$, peaks due to noise dominate the peak CDF and makes the measurement of peak CDF unreliable at this region.

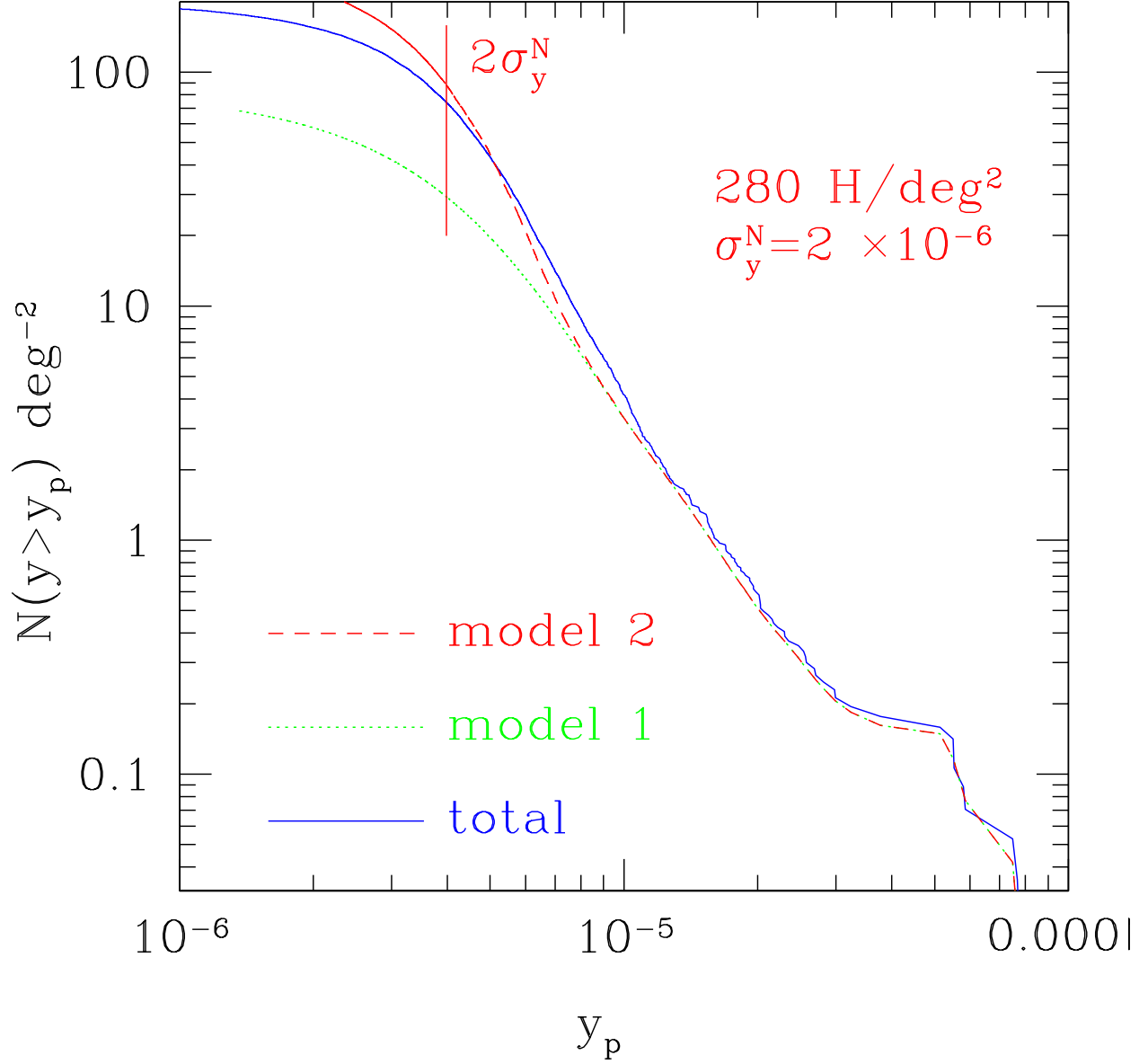


Fig. 15.— Modelled $N(y > y_p)$. The line 'model 1' is calculated from eqn. (10), which consider the effect that noise changes the amplitude of peaks. The line 'model 2' is the sum of 'model 1' and noise peak CDF, which considers the effect that noise introduces false peaks. This result fits the CDF of peaks in the total maps down to $y_p \simeq 2\sigma_y^N$ with better than 30% accuracy.